AEDC-TR-80-24

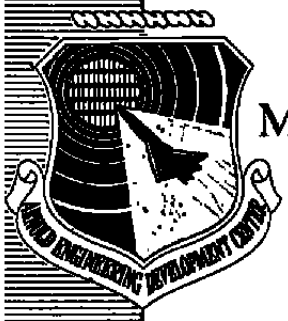

Modifications to MacCormack's 2-D Navier-Stokes Compression Ramp Code for Application to Flows with Axes of Symmetry and Wall Mass Transfer

Richard G. Hindman
ARO, Inc.

January 1981

Final Report for Period January 1979 – March 1980

ARNOLD ENGINEERING DEVELOPMENT CENTER
ARNOLD AIR FORCE STATION, TENNESSEE
AIR FORCE SYSTEMS COMMAND
UNITED STATES AIR FORCE

This report has been reviewed by the Office of Public Affairs (PA) and is releasable to the National Technical Information Service (NTIS). At NTIS, it will be available to the general public, including foreign nations.

APPROVAL STATEMENT

This report has been reviewed and approved.

Elton R Thompson

ELTON R. THOMPSON
Directorate of Technology
Deputy for Operations

Approved for publication:

FOR THE COMMANDER

Marion L. Laster

MARION L. LASTER
Director of Technology
Deputy for Operations

REPORT DOCUMENTATION PAGE		READ INSTRUCTIONS BEFORE COMPLETING FORM
1 REPORT NUMBER AEDC-TR-80-24	2. GOVT ACCESSION NO.	3. RECIPIENT'S CATALOG NUMBER
4. TITLE (and Subtitle) MODIFICATIONS TO MacCORMACK'S 2-D NAVIER-STOKES COMPRESSION RAMP CODE FOR APPLICATION TO FLOWS WITH AXES OF SYMMETRY AND WALL MASS TRANSFER		5 TYPE OF REPORT & PERIOD COVERED Final Report, January 1979 - March 1980 6 PERFORMING ORG. REPORT NUMBER
7 AUTHOR(s) Richard G. Hindman, ARO, Inc., a Sverdrup Corporation Company		8 CONTRACT OR GRANT NUMBER(s)
9 PERFORMING ORGANIZATION NAME AND ADDRESS Arnold Engineering Development Center/DOT Air Force Systems Command Arnold Air Force Station, Tennessee 37389		10 PROGRAM ELEMENT, PROJECT, TASK AREA & WORK UNIT NUMBERS Program Element 65807F
11. CONTROLLING OFFICE NAME AND ADDRESS Arnold Engineering Development Center/DOS Air Force Systems Command Arnold Air Force Station, Tennessee 37389		12 REPORT DATE January 1981 13 NUMBER OF PAGES 54
14 MONITORING AGENCY NAME & ADDRESS(If different from Controlling Office)		15 SECURITY CLASS. (of this report) UNCLASSIFIED 15a DECLASSIFICATION DOWNGRADING SCHEDULE N/A

16 DISTRIBUTION STATEMENT (of this Report)

Approved for public release; distribution unlimited.

17 DISTRIBUTION STATEMENT (of the abstract entered in Block 20, if different from Report)

18 SUPPLEMENTARY NOTES

Available in Defense Technical Information Center (DTIC).

19 KEY WORDS (Continue on reverse side if necessary and identify by block number)

viscosity	fluid dynamics	boundary layer flow
turbulence	control surfaces	Navier-Stokes equations
flow fields	numerical analysis	axisymmetric flow
laminar flow	flared afterbodies	two dimensional flow.
mass transfer	cylindrical bodies	three dimensional flow

20 ABSTRACT (Continue on reverse side if necessary and identify by block number)

A computer code for solving the two-dimensional compressible Navier-Stokes equations governing the supersonic/hypersonic flow over a compression ramp as developed by MacCormack was extended to apply to axisymmetric flows over cylinder-flare shapes. Two new operators were developed for this extension, one of which was found to produce an upper stability bound on the step size. This bound is

DD FORM 1 JAN 73 1473 EDITION OF 1 NOV 65 IS OBSOLETE

20. ABSTRACT (Continued)

proportional to the Prandtl number and inversely proportional to the ratio of thermal capacities of the fluid times the maximum value over all grid points of the kinematic viscosity scaled by the radial coordinate value. Additionally, the computer code was modified to allow for the option of wall mass transfer. This required reformulation of the hyperbolic fine mesh operator because of an assumption in the development of the original operator that the wall-normal velocity in the fine mesh is much less than the sound speed. Numerical results are presented for a particular hollow cylinder-flare configuration, and comparisons are made with the experimental data of Roshko and Thomke and with the results of a boundary-layer code attributable to Patankar and Spalding.

AFSC
Arnold AFS Tenn

PREFACE

The work reported herein was conducted by the Arnold Engineering Development Center (AEDC), Air Force Systems Command (AFSC). The Air Force project manager was Elton R. Thompson, DOT. The results of the research were obtained by ARO, Inc., AEDC Division (a Sverdrup Corporation Company), operating contractor for the AEDC, AFSC, Arnold Air Force Station, Tennessee, under ARO Project No. V32A-01. The manuscript was submitted for publication on May 28, 1980.

The author wishes to thank Dr. J. C. Adams, Mr. J. D. Gray, Dr. A. W. Mayne, Mr. E. S. Powell, Mr. F. L. Shope, and Dr. M. O. Varner for comments and suggestions given during the many enlightening discussions held throughout the course of this work.

CONTENTS

ILLUSTRATIONS

Figure

Figure Page

1.0 INTRODUCTION

Over the past decade, sufficient advances have been made in the field of computational fluid dynamics (CFD) to provide an extremely useful tool to engineering practitioners. This tool is the CFD technology which currently sees extensive use in a large variety of aerospace engineering design and analysis. The present report deals with an extension of this technology which is immediately applicable to the study of flow past specific components of some modern aerospace vehicles.

Consider the wall/ramp arrangement shown in Fig. 1. This two-dimensional configuration may represent a simple model of a vehicle control surface. A ramp-induced shock-boundary-layer interaction results when this model encounters a supersonic/hypersonic airstream. A popular computer code for analyzing this type of problem is documented by Hung and MacCormack (Ref. 1) and by MacCormack (Ref. 2). This code (herein referred to as the original code) solves the Navier-Stokes equations for two-dimensional compressible supersonic/hypersonic laminar flows and for turbulent flows which are adequately described by an algebraic eddy viscosity turbulence model.

The first goal of the present effort was to modify the original code to apply it to the cylinder-flare configuration illustrated in Fig. 2. The desire to compute supersonic/hypersonic flow over cylinder-flare configurations is motivated by the following two considerations. First, such configurations exist in real aerospace applications. The second and perhaps more subtle reason is related to the difficulties encountered with comparing results from the original two-dimensional code to "two-dimensional" experimental data. The "two-dimensional" experimental data suffer from finite span effects which, for turbulent flow, may be important. The *hollow* cylinder-flare eliminates these effects from the experimental data so that less uncertainty exists when experimental data and the appropriate numerical solution are compared. Also, it remains unclear what role, if any, three-dimensional turbulence plays in a "two-dimensional" problem. Because of these considerations, the hollow cylinder-flare configuration should provide a better shape on which to base the design of new turbulence models.

The second goal of the present effort was to install a wall mass transfer option into the computer code which would allow treatment of the hinge-line boundary-layer bleed problem depicted schematically in Fig. 3. This option would also allow treatment of the boundary-layer suction problem which arises frequently in aerospace applications. The boundary-layer suction technique may be used, for example, to enhance control surface effectiveness, etc.

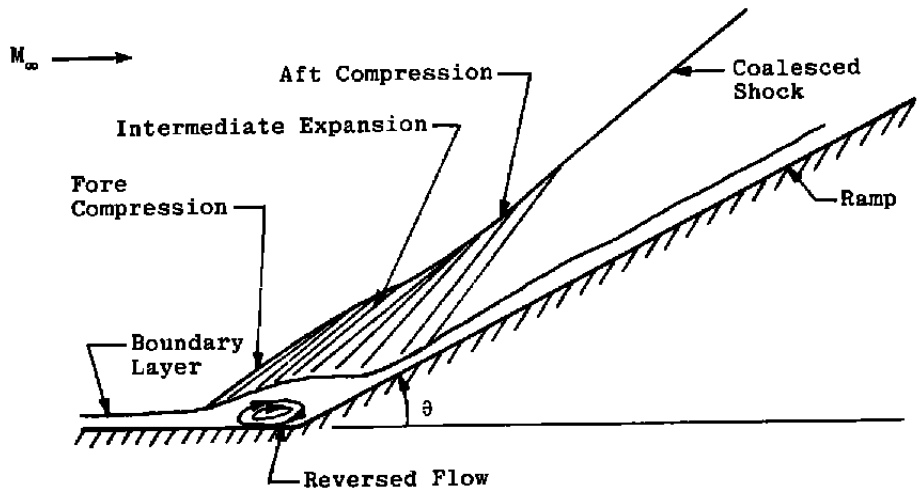

Figure 1. Ramp-induced shock-boundary-layer interaction.

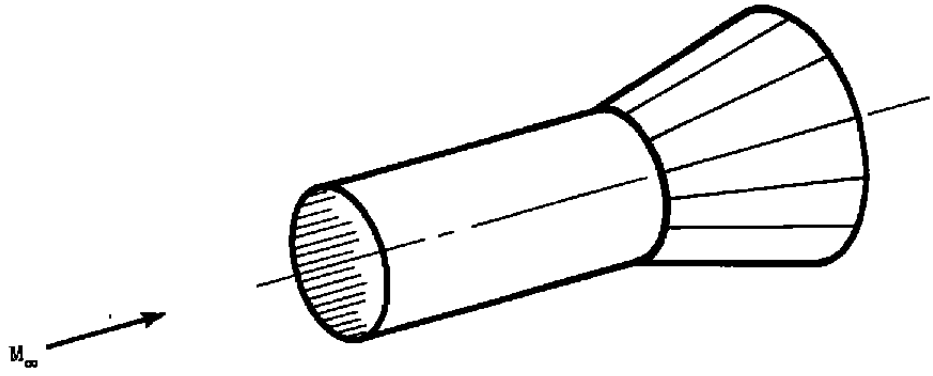

Figure 2. Hollow cylinder-flare configuration.

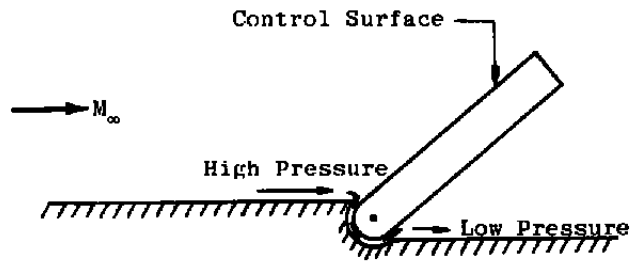

Figure 3. Hinge-line boundary-layer bleed.

Previous investigators have directed a considerable amount of effort toward the study of high-speed shock-boundary-layer interactions. Of primary interest for the present study are investigations of those interactions which are compression corner-induced. Laminar interactions in two dimensions have been studied experimentally by Gray and Rhudy (Ref. 3) and theoretically by Bloy and Georgeff (Ref. 4) and Carter (Ref. 5), for example. Turbulent interactions in two dimensions have been examined experimentally by several investigators including Law (Ref. 6), Settles, Vas, and Bogdonoff (Ref. 7), and Gray and Rhudy (Ref. 3). Investigators of theoretical turbulent interactions include Hung and MacCormack (Ref. 1), Shang and Hankey (Ref. 8), and Coakley, Viegas, and Horstman (Ref. 9). Joint theoretical-experimental turbulent flow efforts have been conducted by various investigators including Horstman, Hung, Settles, Vas, and Bogdonoff (Ref. 10). Much of the theoretical effort in turbulent flows has been devoted to the testing of various types of turbulence models in an attempt to predict with accuracy quantities such as skin friction and heat transfer for separated flows.

Literature on turbulent interactions for axisymmetric flows is not as abundant as for two-dimensional flows. Experimental studies are documented by Kuehn (Ref. 11), Polak and Kalivretenos (Ref. 12), Coleman and Stollery (Ref. 13), and Roshko and Thomke (Ref. 14); however, numerical studies of these interactions using the Navier-Stokes equations are scarce in the literature. It is typical for investigators to study the two-dimensional problems first, and, once these are understood, to extend their investigation to axisymmetric and three-dimensional problems. Even after extensive efforts, two-dimensional turbulent shock-boundary-layer interactions for supersonic/hypersonic flows are not yet fully understood. Therefore, it may be necessary in this case to focus first on the axisymmetric problem due to the very nature of turbulence. At least part of the difficulty in understanding this type of flow is attributable to the lack of understanding of the magnitude to which turbulence levels are influenced by three-dimensional effects such as the finite span effects previously mentioned. This is not to say that a concentrated effort on the axisymmetric problem will yield all the answers, but rather that there may well be fewer unknowns with which to deal.

The additional complication of wall mass transfer for flat plates has received extensive experimental and numerical study; however, the numerical approaches typically involve the boundary-layer equations. The present work illustrates how the wall mass transfer idea is applied to the complete Navier-Stokes equations for compression corner-induced shock-boundary-layer interactions.

The organization of the remainder of this report is now described. Section 2.0 deals with the governing equations, the axisymmetric assumption, the approximations inherent in the turbulent flow equations, and an assessment of these approximations for some of the applications of interest. This section also contains a description of two algebraic eddy viscosity turbulence models used in the present work. Section 3.0 deals with the numerical aspects of incorporating the axisymmetric assumption into the existing computer code. Specific topics addressed include the finite-difference grid, the time-splitting approach, and stability of the resulting source term operators. A description of the analysis and numerical application involved in generalizing the boundary conditions to include the effectss of wall mass transfer is included in Section 4.0. Section 5.0 contains comparisons of numerical results with experimental data which verify the resulting computer code for a certain class of problems and illustrate its deficiencies for another class of problems. A discussion of the code's potential, as well as its deficiencies, is also presented. Section 6.0 contains concluding remarks.

2.0 GOVERNING EQUATIONS

2.1 THREE-DIMENSIONAL NAVIER-STOKES EQUATIONS

The fully three-dimensional time-dependent Navier-Stokes equations are given in conservation-law form by

$$\frac{\partial \bar{\phi}}{\partial t} + \frac{\partial \bar{e}}{\partial x} + \frac{\partial \bar{f}}{\partial y} + \frac{\partial \bar{g}}{\partial z} = 0 \tag{1}$$

where

$$\bar{e} = \bar{e}_i - \bar{e}_v \ , \ \bar{f} = \bar{f}_i - \bar{f}_v \ , \ \bar{g} = \bar{g}_i - \bar{g}_v$$

and the barred quantities indicate an association with the Cartesian reference frame. The subscripts i and v denote inviscid and viscous contributions, respectively. The quantities $\bar{e}_i$, $\bar{f}_i$, and $\bar{g}_i$ are given by

$$\bar{e}_i = \begin{pmatrix} \rho\bar{u} \\ p - \rho\bar{u}^2 \\ \rho\bar{u}\,\bar{v} \\ \rho\bar{u}\,\bar{w} \\ (\epsilon + p)\bar{u} \end{pmatrix}, \quad \bar{f}_i = \begin{pmatrix} \rho\bar{v} \\ \rho\bar{v}\,\bar{u} \\ p + \rho\bar{v}^2 \\ \rho\bar{v}\,\bar{w} \\ (\epsilon + p)\bar{v} \end{pmatrix}, \quad \bar{g}_i = \begin{pmatrix} \rho\bar{w} \\ \rho\bar{w}\,\bar{u} \\ \rho\bar{w}\,\bar{v} \\ p + \rho\bar{w}^2 \\ (\epsilon + p)\bar{w} \end{pmatrix}$$

and $\bar{e}_v$, $\bar{f}_v$, $\bar{g}_v$ are given by

$$\bar{e}_v = \begin{pmatrix} 0 \\ \left(\kappa - \frac{2}{3}\mu\right)\nabla \cdot \vec{q} + \mu\hat{i} \cdot \left(\frac{\partial \vec{q}}{\partial x} + \nabla\bar{u}\right) \\ \mu\hat{j} \cdot \left(\frac{\partial \vec{q}}{\partial x} + \nabla\bar{u}\right) \\ \mu\hat{k} \cdot \left(\frac{\partial \vec{q}}{\partial x} + \nabla\bar{u}\right) \\ \left(\kappa - \frac{2}{3}\mu\right)(\nabla \cdot \vec{q})\,\bar{u} + \mu\vec{q} \cdot \left(\frac{\partial \vec{q}}{\partial x} + \nabla\bar{u}\right) + k\frac{\partial T}{\partial x} \end{pmatrix}$$

$$\bar{f}_v = \begin{pmatrix} 0 \\ \mu\hat{i} \cdot \left(\frac{\partial \vec{q}}{\partial y} + \nabla\bar{v}\right) \\ \left(\kappa - \frac{2}{3}\mu\right)\nabla \cdot \vec{q} + \mu\hat{j} \cdot \left(\frac{\partial \vec{q}}{\partial y} + \nabla\bar{v}\right) \\ \mu\hat{k} \cdot \left(\frac{\partial \vec{q}}{\partial y} + \nabla\bar{v}\right) \\ \left(\kappa - \frac{2}{3}\mu\right)(\nabla \cdot \vec{q})\,\bar{v} + \mu\vec{q} \cdot \left(\frac{\partial \vec{q}}{\partial y} + \nabla\bar{v}\right) + k\frac{\partial T}{\partial y} \end{pmatrix}$$

$$\bar{g}_v = \begin{pmatrix} 0 \\ \mu \hat{i} \cdot \left(\frac{\partial \vec{q}}{\partial z} + \nabla \bar{w} \right) \\ \mu \hat{j} \cdot \left(\frac{\partial \vec{q}}{\partial z} - \nabla \bar{w} \right) \\ \left(\kappa - \frac{2}{3} \mu \right) \nabla \cdot \vec{q} + \mu \hat{k} \cdot \left(\frac{\partial \vec{q}}{\partial z} + \nabla \bar{w} \right) \\ \left(\kappa - \frac{2}{3} \mu \right) (\nabla \cdot \vec{q}) \bar{w} + \mu \vec{q} \cdot \left(\frac{\partial \vec{q}}{\partial z} + \nabla \bar{w} \right) + k \frac{\partial T}{\partial z} \end{pmatrix}$$

The solution vector $\bar{\phi}$ is given by

$$\bar{\phi} = \begin{pmatrix} \rho \\ \rho \bar{u} \\ \rho \bar{v} \\ \rho \bar{w} \\ \epsilon \end{pmatrix}$$

In these equations, μ is the dynamic or first coefficient of viscosity, $\lambda = \kappa - 2/3\ \mu$ is the second coefficient of viscosity* (actually, as is typically done in practice, κ, the bulk viscosity coefficient,* is taken to be zero), k is the thermal conductivity of the fluid, ϵ is the total energy per unit volume of the fluid and is related to pressure, p, density, ϱ, and (x, y, z) velocity components, ($\bar{u}$, $\bar{v}$, $\bar{w}$), by the equation

$$\epsilon = \frac{p}{\gamma - 1} - \frac{\rho}{2} \left(\bar{u}^2 + \bar{v}^2 - \bar{w}^2 \right)$$

assuming the fluid behaves according to the perfect gas law $p = (\gamma - 1) \varrho\, \tilde{e}$ where $\tilde{e}$ is the specific internal energy of the fluid. In addition, T is the static temperature of the fluid, $\vec{q}$ is the velocity vector, ($\hat{i}$, $\hat{j}$, $\hat{k}$) are the Cartesian unit vectors in the (x, y, z) directions, respectively, and ∇ is the gradient operator.

*The notation and definitions advocated by Rosenhead (Ref. 15) and used by Owczarek (Ref. 16) are employed here. These differ from those used by Lamb (Ref. 17) and Yuan (Ref. 18).

2.2 THE AXISYMMETRIC ASSUMPTION

To treat the axisymmetric flow case it is necessary to introduce a more general set of independent variables. Let

$$\tau = t$$

$$\xi = x$$

$$\eta = \eta(y, z)$$

$$\zeta = \zeta(y, z)$$

Equation (1) may be rewritten in terms of these independent variables to yield

$$\frac{\partial \bar{\phi}}{\partial \tau} + \frac{\partial \bar{e}}{\partial \xi} + \frac{\partial}{\partial \eta}\left(\eta_y \bar{f} + \eta_z \bar{g}\right) + \frac{\partial}{\partial \zeta}\left(\zeta_y \bar{f} + \zeta_z \bar{g}\right) - \left[(\eta_y)_\eta + (\zeta_y)_\zeta\right]\bar{f} - \left[(\eta_z)_\eta + (\zeta_z)_\zeta\right]\bar{g} = 0 \tag{2}$$

These independent variables are made to look like cylindrical coordinates by introducing the rotation

$$y = \eta \cos\zeta$$

$$z = \eta \sin\zeta$$

from which the following relations are obtained:

$$\eta_y = \cos\zeta \quad , \quad \eta_z = \sin\zeta \quad , \quad \zeta_y = -\frac{\sin\zeta}{\eta} = -\frac{\eta_z}{\eta}$$

$$\zeta_z = \frac{\cos\zeta}{\eta} = \frac{\eta_y}{\eta} \quad , \quad (\eta_y)_\eta = 0 \quad , \quad (\zeta_y)_\zeta = -\frac{\cos\zeta}{\eta} = -\frac{\eta_y}{\eta} = -\zeta_z$$

$$(\eta_z)_\eta = 0 \quad , \quad (\zeta_z)_\zeta = -\frac{\sin\zeta}{\eta} = -\frac{\eta_z}{\eta} = \zeta_y$$

The use of these relations in Eq. (2) produces a repeated occurrence of the groupings $(\eta_y \bar{f} + \eta_z \bar{g})$ and $(\eta_y \bar{g} - \eta_z \bar{f})$. Since the cylindrical (ξ, η, ζ) velocity components (u, v, w) are related to the Cartesian components by

$$u = \bar{u}$$

$$v = \eta_y \bar{v} + \eta_z \bar{w}$$

$$w = \eta_y \bar{w} - \eta_z \bar{v}$$

it is a simple geometric exercise to show that replacing the third component of Eq. (2) by η_z times the fourth component plus η_y times the third component, and replacing the fourth component of Eq. (2) by η_y times the fourth component minus η_z times the third component yields the Navier-Stokes equations in cylindrical coordinates:

$$\frac{\partial \hat{\phi}}{\partial \tau} + \frac{\partial \hat{e}}{\partial \xi} + \frac{\partial \hat{f}}{\partial \eta} + \frac{\partial \hat{g}}{\partial \zeta} + \hat{h} = 0$$

where

$$\hat{\phi} = (\rho \ , \ \rho u \ , \ \rho v \ , \ \rho w \ , \ \epsilon)^{T^*} \ , \ \hat{e} = \hat{e}_i - \hat{e}_v \ , \ \hat{f} = \hat{f}_i - \hat{f}_v \ ,$$

$$\hat{g} = \hat{g}_i - \hat{g}_v \ , \ \hat{h} = \hat{h}_i - \hat{h}_v \ \text{ and } \ \hat{e}_i \ , \ \hat{f}_i \ , \ \hat{g}_i \ , \ \hat{h}_i$$

are given by

$$\hat{e}_i = \begin{pmatrix} \rho u \\ p + \rho u^2 \\ \rho u v \\ \rho u w \\ (\epsilon + p) u \end{pmatrix} \ , \ \hat{f}_i = \begin{pmatrix} \rho v \\ \rho v u \\ p - \rho v^2 \\ \rho v w \\ (\epsilon + p) v \end{pmatrix} \ ,$$

$$\hat{g}_i = \frac{1}{\eta} \begin{pmatrix} \rho w \\ \rho u w \\ \rho v w \\ p + \rho w^2 \\ (\epsilon - p) w \end{pmatrix} \ , \ \hat{h}_i = \frac{1}{\eta} \begin{pmatrix} \rho v \\ \rho v u \\ \rho (v^2 - w^2) \\ 2 \rho v w \\ (\epsilon + p) v \end{pmatrix}$$

*The superscript T denotes the transpose operation.

with $\hat{e}_v$, $\hat{f}_v$, $\hat{g}_v$, $\hat{h}_v$ given by

$$\hat{e}_v = \begin{pmatrix} 0 \\ \lambda(\nabla \cdot \vec{q}) + \mu \hat{i}_\xi \cdot \left(\frac{\partial \vec{q}}{\partial \xi} + \nabla u\right) \\ \mu \hat{i}_\eta \cdot \left(\frac{\partial \vec{q}}{\partial \xi} + \nabla u\right) \\ \mu \hat{i}_\zeta \cdot \left(\frac{\partial \vec{q}}{\partial \xi} + \nabla u\right) \\ \lambda(\nabla \cdot \vec{q}) u + \mu \vec{q} \cdot \left(\frac{\partial \vec{q}}{\partial \xi} + \nabla u\right) + k \frac{\partial T}{\partial \xi} \end{pmatrix}$$

$$\hat{f}_v = \begin{pmatrix} 0 \\ \mu \hat{i}_\xi \cdot \left(\frac{\partial \vec{q}}{\partial \eta} + \nabla v\right) \\ \lambda(\nabla \cdot \vec{q}) + \mu i_\eta \cdot \left(\frac{\partial \vec{q}}{\partial \eta} + \nabla v\right) \\ \mu \hat{i}_\zeta \cdot \left(\frac{\partial \vec{q}}{\partial \eta} + \nabla v\right) \quad \left(-\mu \frac{w}{\eta}\right) \\ \lambda(\nabla \cdot \vec{q}) v + \mu \vec{q} \cdot \left(\frac{\partial \vec{q}}{\partial \eta} + \nabla v\right) + k \frac{\partial T}{\partial \eta} \quad \left(-\mu \frac{w^2}{\eta}\right) \end{pmatrix}$$

$$\hat{g}_v = \frac{1}{\eta} \begin{pmatrix} 0 \\ \mu \hat{i}_\xi \cdot \left(\frac{1}{\eta} \frac{\partial \vec{q}}{\partial \zeta} - \nabla w\right) \\ \mu \hat{i}_\eta \cdot \left(\frac{1}{\eta} \frac{\partial \vec{q}}{\partial \zeta} + \nabla w\right) \quad \left(-\mu \frac{w}{\eta}\right) \\ \lambda(\nabla \cdot \vec{q}) + \mu \hat{i}_\zeta \cdot \left(\frac{1}{\eta} \frac{\partial \vec{q}}{\partial \zeta} + \nabla w\right) \quad \left(+2\mu \frac{v}{\eta}\right) \\ \lambda(\nabla \cdot \vec{q}) w + \mu \vec{q} \cdot \left(\frac{1}{\eta} \frac{\partial \vec{q}}{\partial \zeta} + \nabla w\right) + k \frac{1}{\eta} \frac{\partial T}{\partial \zeta} \quad \left(+\mu \frac{v w}{\eta}\right) \end{pmatrix}$$

$$\hat{h}_v = \frac{1}{\eta}\begin{pmatrix} 0 \\ \mu\hat{i}_\xi \cdot \left(\frac{\partial\vec{q}}{\partial\eta} + \nabla v\right) \\ \mu\hat{i}_\eta \cdot \left(\frac{\partial\vec{q}}{\partial\eta} + \nabla v\right) - \mu\hat{i}_\zeta \cdot \left(\frac{1}{\eta}\frac{\partial\vec{q}}{\partial\zeta} + \nabla w\right) - 2\mu\frac{v}{\eta} \\ 2\mu\hat{i}_\zeta \cdot \left(\frac{\partial\vec{q}}{\partial\eta} + \nabla v\right) - 2\mu\frac{w}{\eta} \\ \lambda(\nabla\cdot\vec{q})v + \mu\vec{q}\cdot\left(\frac{\partial\vec{q}}{\partial\eta} - \nabla v\right) - \mu\frac{w^2}{\eta} + k\frac{\partial T}{\partial\eta} \end{pmatrix}$$

where $\hat{i}_\xi$, $\hat{i}_\eta$, $\hat{i}_\zeta$ are the cylindrical unit vectors in the direction indicated by the subscripts. These equations look like their counterparts in the Cartesian reference frame except for the appearance of the source terms $\hat{h}_i$ and $\hat{h}_v$ and the terms encircled by dotted lines in the expressions for $\hat{f}_v$ and $\hat{g}_v$.

If the problems of interest are restricted to nonspinning bodies of revolution at zero incidence, then the meridional velocity and its gradient are zero. In this case the ζ-momentum equation is trivially satisfied and the remaining system of equations is given by

$$\frac{\partial\phi}{\partial t} + \frac{\partial e}{\partial x} + \frac{\partial f}{\partial y} + h = 0 \tag{3}$$

where the independent variables (t, x, y) have been re-introduced for readability with the obvious associations

$$\tau \leftarrow t \ , \ \xi \leftarrow x \ , \ \eta \leftarrow y \ , \ \hat{i}_\xi \leftarrow \hat{i} \ , \ \hat{i}_\eta \leftarrow \hat{j}$$

The quantities ϕ, e, f, and h are given by $\phi = (\varrho, \varrho u, \varrho v, \epsilon)^T$; $e = e_i - e_v$; $f = f_i - f_v$, and $h = h_i - h_v$ where

$$e_i = \begin{pmatrix} \rho u \\ p + \rho u^2 \\ \rho uv \\ (\epsilon + p)u \end{pmatrix}, \quad f_i = \begin{pmatrix} \rho v \\ \rho vu \\ p + \rho v^2 \\ (\epsilon + p)v \end{pmatrix}, \quad h_i = \frac{1}{y}\begin{pmatrix} \rho v \\ \rho vu \\ \rho v^2 \\ (\epsilon + p)v \end{pmatrix}$$

and

$$e_v = \begin{pmatrix} 0 \\ \lambda(\nabla \cdot \vec{q}) + \mu\hat{i} \cdot \left(\frac{\partial \vec{q}}{\partial x} + \nabla u\right) \\ \mu\hat{j} \cdot \left(\frac{\partial \vec{q}}{\partial x} + \nabla u\right) \\ \lambda(\nabla \cdot \vec{q})\, u + \mu\vec{q} \cdot \left(\frac{\partial \vec{q}}{\partial x} + \nabla u\right) + k\frac{\partial T}{\partial x} \end{pmatrix} \tag{4}$$

$$f_v = \begin{pmatrix} 0 \\ \mu\hat{i} \cdot \left(\frac{\partial \vec{q}}{\partial y} + \nabla v\right) \\ \lambda(\nabla \cdot \vec{q}) + \mu\hat{j} \cdot \left(\frac{\partial \vec{q}}{\partial y} + \nabla v\right) \\ \lambda(\nabla \cdot \vec{q})\, v + \mu\vec{q} \cdot \left(\frac{\partial \vec{q}}{\partial y} + \nabla v\right) + k\frac{\partial T}{\partial y} \end{pmatrix} \tag{5}$$

$$h_v = \frac{1}{y} \begin{pmatrix} 0 \\ \mu\hat{i} \cdot \left(\frac{\partial \vec{q}}{\partial y} + \nabla v\right) \\ \mu\hat{j} \cdot \left(\frac{\partial \vec{q}}{\partial y} + \nabla v\right) - 2\mu\frac{v}{y} \\ \lambda(\nabla \cdot \vec{q})\, v + \mu\vec{q} \cdot \left(\frac{\partial \vec{q}}{\partial y} + \nabla v\right) + k\frac{\partial T}{\partial y} \end{pmatrix} \tag{6}$$

These equations appear to be identical to their two-dimensional Cartesian counterparts except for the source term, h. There is also the hidden difference in the velocity divergence term, $\nabla.\vec{q}$, which for the axisymmetric case, is given by

$$\nabla \cdot \vec{q} = \frac{\partial u}{\partial x} + \frac{\partial v}{\partial y} + \frac{v}{y} \tag{7}$$

As is demonstrated in Section 3.0, this similarity between the two-dimensional Cartesian and the axisymmetric equations allows the axisymmetric assumption to be incorporated into the original two-dimensional computer code as a pair of source term operators in the already present time-split operator sequence.

2.3 TURBULENCE MODELING

2.3.1 Concepts and Assumptions

It is generally accepted that the Navier-Stokes equations are applicable to both laminar and turbulent flows (Ref. 19). It is unfortunate, however, that the small significant length scales present in turbulent flows render the numerical simulation of such flows impractical with regard to resolving these scales on current computer architecture. It is therefore necessary to employ some type of modeling procedure to compute turbulent flows.

The mass-weighted averaging technique usually associated with compressible flows is used in the present approach. A description of this technique is given by Marvin (Ref. 19). The key feature of this method is that there are fewer terms representing the so-called turbulent Reynolds stresses and heat fluxes than for the Reynolds averaging method. The modeling problem may thus be reduced to a problem of representing these stresses and heat fluxes in terms of the mean and mass-weighted flow variables. One approach is to use the classical Boussinesq assumption, which provides a simple means to simulate the *effect* of turbulence through an eddy viscosity formulation where the μ appearing in Eqs. (4) through (6) is simply taken to be the sum of a laminar contribution, μ_ℓ, and a turbulent contribution, μ_t. The laminar viscosity is assumed to be governed by Sutherland's Law given by

$$\mu_\ell = 2.27\,(10)^{-8}\,\frac{T^{3/2}}{T + 198.6}$$

where the static temperature, T, is in degrees Rankine. The turbulent viscosity is determined from a two-layer model to be discussed later. A treatment of the heat flux terms of Eqs. (4) through (6) uses the definition of Prandtl number, Pr_ℓ, and the introduction of a turbulent Prandtl number, Pr_t

$$Pr_\ell = \frac{\mu_\ell c_p}{k_\ell}\ ,\quad Pr_t = \frac{\mu_t c_p}{k_t}$$

where c_p is the specific heat at constant pressure. The conductivity, k, in Eqs. (4) through (6) is then given by

$$k = k_\ell + k_t = c_p\left(\frac{\mu_\ell}{Pr_\ell} + \frac{\mu_t}{Pr_t}\right)$$

where both Pr_ℓ and Pr_t are assumed to have constant values of 0.72 and 0.9, respectively.

As mentioned, the turbulent viscosity is modeled with a two-layer concept. The basic inner layer model uses Prandtl's mixing-length hypothesis and is given by

$$(\mu_t)_{inner} = \rho \ell^2 (y) G \tag{8}$$

where ρ is the local mean density, $\ell(y) = \hat{k}\, y\, D$ where $\hat{k}$ is a constant usually taken to be 0.4, and D is the van Driest damping factor given by

$$D = 1 - e^{-\frac{y^+}{A^+}}$$

where $y^+ = y \frac{\sqrt{\rho_r \tau_r}}{\mu_r}$ and A^+ may be used to incorporate the effects of streamwise pressure gradient and wall mass transfer similar to its use in incompressible flows as indicated by Marvin (Ref. 19). The subscript r appearing in the definition of y^+ denotes a reference condition evaluated at the wall point. G denotes some measure of the local mass-weighted velocity gradient.

The outer layer model is given by

$$(\mu_t)_{outer} = C \hat{y} \rho\, Q(y) \tag{9}$$

where C is a constant, $\hat{y}$ is a reference distance normal to the wall, and Q(y) is a Klebanoff-type intermittency factor given by

$$Q(y) = \left[1 + 5.5\,(by)^6\right]^{-1} \tag{10}$$

where b is a constant.

In practice, $(\mu_t)_{inner}$ is used out to the first point where it exceeds $(\mu_t)_{outer}$, and $(\mu_t)_{outer}$ is used from this point out to the edge of the turbulent layer.

At this point a brief summary is given of the basic turbulence-related assumptions inherent in the mass-weighted averaged Navier-Stokes equations used in the present work:

1. It is assumed that the goal is only to determine the mass-weighted and/or mean variables, since the averaging process precludes the reconstruction of the original dependent variables (i.e., a loss of information is accepted).

2. Reynolds stresses and turbulent heat flux have the same form as the conventional laminar stress tensor and laminar heat flux, respectively.

3. The laminar and turbulent Prandtl numbers are assumed to be constant and their values are taken to be 0.72 and 0.9, respectively.

4. The eddy viscosity may be represented by a simple two-layer algebraic model of the type previously described.

Although all of these assumptions limit the applicability of the given equations, probably the most restrictive of all are assumptions 2 and 4. Efforts are underway by various investigators to relax these two assumptions somewhat by developing more rigorous and more complex methods to evaluate the Reynolds stresses and turbulent heat flux terms. These methods attempt to model more fundamental properties of the turbulent flow and are referred to as multi-equation models.

2.3.2 Current Model

The model existing within the original computer code is referred to as the current model. This model is styled after one by Cebeci, Smith, and Mosinskis (Ref. 20), with G in Eq. (8) given by

$$G = \left| \frac{\partial u}{\partial v} \right|$$

where u is the component of mass-weighted velocity normal to the y direction and y is measured normal to the wall. C, $\hat{y}$, and b in Eqs. (9) and (10) are given by

$$C = Ku_e$$

$$\hat{y} = \delta^* = \int_0^{\delta} \left(1 - \frac{u}{u_e}\right) dy$$

$$b = \frac{1}{\delta}$$

where δ is the boundary-layer thickness, u_e is the velocity at the boundary-layer edge, and K is an empirical constant set at 0.0168. Unfortunately, this model requires that a boundary-layer edge be clearly distinguishable, which is not the case for many flows with shock-boundary- layer interactions, including separated flows.

2.3.3 Alternate Model

An alternate model is one developed by Baldwin and Lomax (Ref. 21), with G in Eq. (8) given by

$$G = |\omega| = |\nabla \times \vec{q}|$$

and C, $\hat{y}$, and b in Eqs. (9) and (10) given by

$$C = K\,C_{CP}$$

$$\hat{y} = F_{WAKE}$$

$$b = C_{KLEB}/y_{MAX}$$

F_{WAKE} is the minimum of $y_{MAX}\,F_{MAX}$ and $C_{WK}y_{MAX}\,U^2_{DIF}/F_{MAX}$ where F_{MAX} is the maximum value of the function

$$F(y) = y|\omega|D$$

and y_{MAX} is the location at which F_{MAX} occurs. U_{DIF} is defined by

$$U_{DIF} = \left(\sqrt{u^2 + v^2}\right)_{MAX} - \left(\sqrt{u^2 + v^2}\right)_{MIN}$$

and the constants, C_{CP}, C_{KLEB}, and C_{WK} are set by Baldwin and Lomax to the values

$$C_{CP} = 1.6$$

$$C_{KLEB} = 0.3$$

$$C_{WK} = 0.25$$

Note that this model does not require the determination of a boundary-layer edge.

Many variations exist in the two models just described but the worthiness of any of these models is a function of the particular problem being solved.

3.0 NUMERICAL INCORPORATION OF THE AXISYMMETRIC ASSUMPTION

3.1 FINITE-DIFFERENCE GRID AND BOUNDARY CONDITIONS

As mentioned in the introduction and illustrated in Fig. 1, the original computer code was designed for a specific class of problems — namely two-dimensional wall-ramp configurations. The purpose of this section is to illustate how an extension was made to allow treatment of the cylinder-flare configuration shown in Fig. 2. The basic physical domain appears identical to its two-dimensional counterpart since only one plane of the axisymmetric problem is required. The finite-difference grid depicted in Fig. 4, therefore, is identical to that documented by Hung and MacCormack (Ref. 1). This is a double layer grid with the first layer indicated by the height, H_F. The grid lines in this layer are highly clustered near the wall. This layer is called the fine mesh and is intended to contain all of the

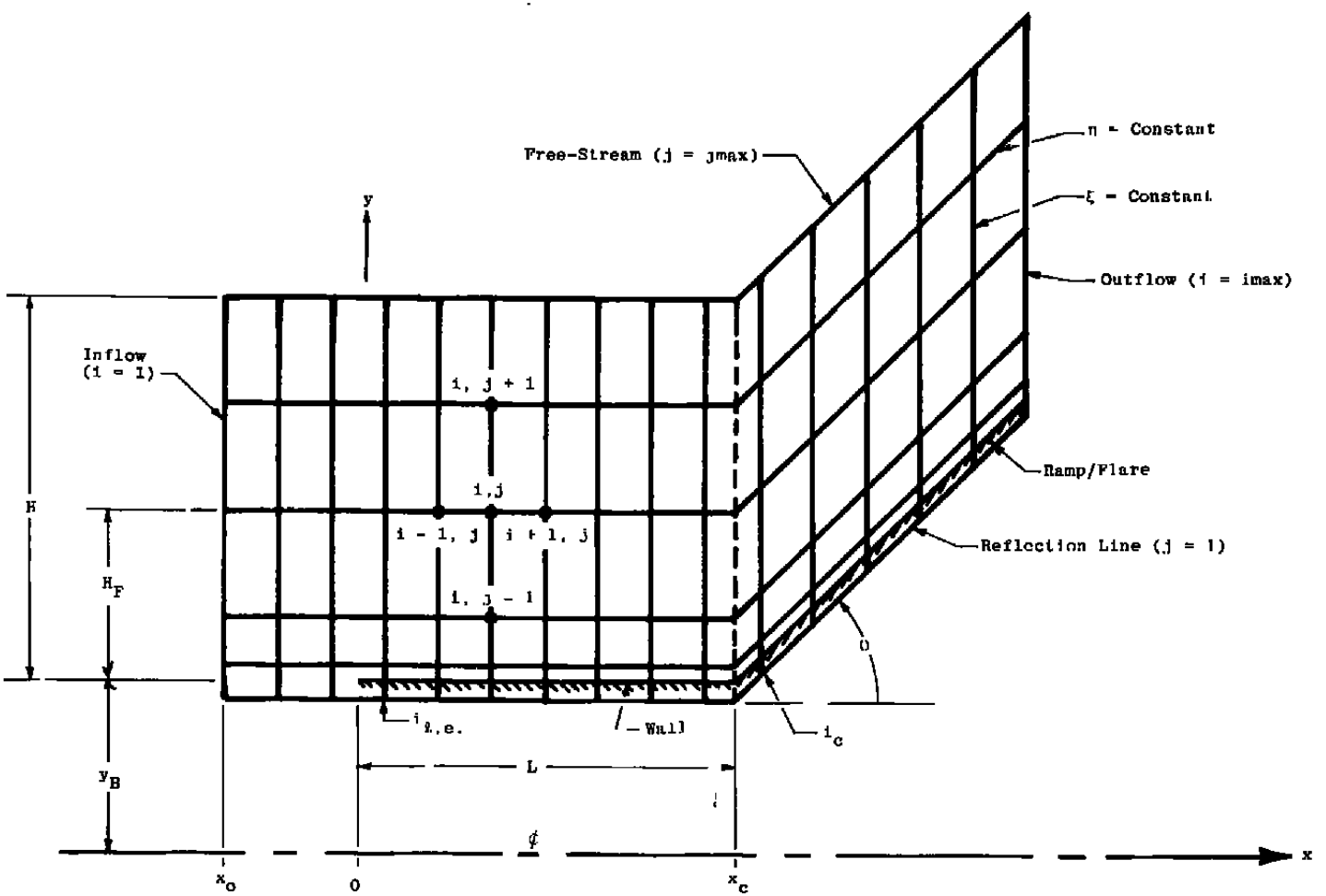

Figure 4. Representative finite-difference grid.

viscous interaction of the problem including the boundary layer and the separation zone, if one exists. The outer layer, or coarse mesh, extends from the outer edge of the fine mesh to a height, H, above the wall. This layer is intended to contain the inviscid features of the flow such as leading edge shocks or bow shocks. The outer edge of this layer is presumed to be in the free-stream flow region. The grid point indices are (i, j) as indicated in the figure.

One final point to be made with reference to Fig. 4 concerns the application of boundary conditions on this grid. The upper boundary conditions are fixed at the free-stream flow values. The left boundary condition is fixed at some known inflow solution. The right boundary requires some type of simulation of an outflow condition. This is accomplished by a simple extrapolation of the solution along j = constant grid lines. The lower grid boundary is used as a reflection line to simulate the existence of a solid boundary. The problem here is to determine the primitive variables (p, T, u, v) at points (i, 1) based on known or assumed properties of viscous flow at solid boundaries. With reference again to Fig. 4, points ahead of the solid wall (if there are any) where $i < i_{l.e.}$ are treated very simply by

$$\begin{aligned} p_{i,1} &= p_{i,2} \\ T_{i,1} &= T_{i,2} \\ u_{i,1} &= u_{i,2} \\ v_{i,1} &= -v_{i,2} \end{aligned} \tag{11}$$

The points where $i \geq i_{l.e.}$ are handled by applying the no-slip velocity condition

$$\begin{aligned} u_{i,1} &= -u_{i,2} \\ v_{i,1} &= -v_{i,2} \end{aligned} \tag{12}$$

and by assuming either a fixed wall temperature, T_w, such that

$$T_{i,1} = 2T_w - T_{i,2} \tag{13}$$

or an adiabatic wall condition such that

$$T_{i,1} = \left[1 - f(\theta_i)\right] T_{i,2} + f(\theta_i)\, T_{i-1,2} \tag{14}$$

where $f(\phi_i) = \sin\phi_i \cos\phi_i\, (y_{i,2}-y_{i,1})/(x_i-x_{i-1})$ and ϕ_i is given by

$$\theta_i = \begin{cases} 0 & \text{for } i < i_c \\ \theta & \text{for } i \geq i_c \end{cases} \tag{15}$$

The remaining variable $p_{i,1}$ is determined by solving a finite-difference approximation to the steady form of the y-momentum equation* applied at the solid boundary. This equation is obtained by performing a coordinate mapping on Eq. (3) so the new computational coordinate lines are as indicated in Fig. 4. This is accomplished by introducing the computational coordinates (τ, ξ, η) defined as

$$\tau = t$$

$$\xi = x$$

$$\eta = \begin{cases} y - y_B & \text{for } x < x_c \\ y - y_B - (x - x_c)\tan\theta & \text{for } x \geq x_c \end{cases}$$

Application of this mapping to Eq. (3) yields

$$\frac{\partial \phi}{\partial \tau} + \frac{\partial o}{\partial \xi} + \frac{\partial}{\partial \eta}(f + \eta_x e) - h = 0 \tag{16}$$

where

$$\eta_x = \begin{cases} 0 & \text{for } x < x_c \\ -\tan\theta & \text{for } x \geq x_c \end{cases} \quad \text{or} \quad \eta_x = -\tan\theta(x)$$

where

$$\theta(x) = \begin{cases} 0 & \text{for } x < x_c \\ \theta & \text{for } x \geq x_c \end{cases}$$

The pressure is then obtained by setting $\phi_\tau = 0$ and solving the third component of Eq. (16) for p_η. The result is

$$\begin{aligned} \frac{\partial p}{\partial \eta} = {} & \left[-\rho v (v + \eta_x u) - \mu (v + \eta_x u)_\eta - \mu \eta_x v_\xi + \mu \left(1 + \eta_x^2\right) v_\eta + \lambda u_\xi - \lambda (v + \eta_x u)_\eta \right]_\eta \\ & + \left[-\rho u v + \mu u_\eta + \mu v_\xi + \mu \eta_x v_\eta \right]_\xi - \frac{1}{y} \left[(\lambda v)_\eta + 2\mu v_\eta - \rho v^2 \right] - \frac{1}{y^2} \left[(\lambda - 2\mu) v \right] \end{aligned} \tag{17}$$

This equation has the form p_η = right-hand side (RHS) where RHS is evaluated at the solid boundary. If p_η is approximated by a central difference, the quantity $p_{i,1}$ is obtained from

---

*The use of the steady form of the normal momentum equation is valid for unsteady flows since the $\partial/\partial t$ term involves only the time variation of the wall-normal mass flux. This variation is zero for time-variant wall mass transfer.

$$P_{i,1} = P_{i,2} - (y_2 - y_1)\ \mathrm{RHS} \tag{18}$$

It should be noted that for the specific case where $u = v = 0$ at the solid boundary (no-slip and no mass transfer), many of the terms in RHS vanish.

3.2 TIME-SPLITTING APPROACH

The time-splitting approach of MacCormack (Ref. 2), also known as the method of fractional steps, is used in the original computer code to solve the two-dimensional counterpart of Eq. (16).

A complex multidimensional partial differential equation may be split into a sequence of simpler one-dimensional equations, each of which is then approximated by finite-differences. Then a simple sequence of various one-dimensional operators yields successive candidate solutions of which the final one approximates the solution to the multidimensional equation. This allows consideration of various terms or groups of terms separately. For example, consider the two-dimensional equation in computational coordinates

$$\frac{\partial \Phi}{\partial \tau} + \frac{\partial E}{\partial \xi} + \frac{\partial F}{\partial \eta} = 0$$

where $\Phi = \phi$, $E = e$, $F = f + \eta_x e$ and ϕ, e, f are the same as those appearing in Eq. (3). The solution to this equation may be obtained by applying the following sequence of operators:

$$L_\xi\left(\frac{\Delta\tau}{2}\right)\begin{cases} \Phi^{\bar{a}} = \Phi^n - \dfrac{\Delta\tau}{2} E^n_\xi \\ \Phi^a = \dfrac{1}{2}\left(\Phi^{\bar{a}} + \Phi^n - \dfrac{\Delta\tau}{2} E^{\bar{a}}_\xi\right) \end{cases}$$

$$L_\eta(\Delta\tau)\begin{cases} \Phi^{\bar{b}} = \Phi^a - \Delta\tau F^a_\eta \\ \Phi^b = \dfrac{1}{2}\left(\Phi^{\bar{b}} + \Phi^a - \Delta\tau F^{\bar{b}}_\eta\right) \end{cases}$$

$$L_\xi\left(\frac{\Delta\tau}{2}\right)\begin{cases} \Phi^{\overline{n+1}} = \Phi^b - \dfrac{\Delta\tau}{2} E^b_\xi \\ \Phi^{n+1} = \dfrac{1}{2}\left(\Phi^{\overline{n+1}} + \Phi^b - \dfrac{\Delta\tau}{2} E^{\overline{n+1}}_\xi\right) \end{cases}$$

so that in operational notation

$$\Phi^{n+1} = L_\xi\left(\frac{\Delta\tau}{2}\right) L_\eta(\Delta\tau)\, L_\xi\left(\frac{\Delta\tau}{2}\right) \Phi^n \tag{19}$$

The operator L_ξ is applied twice to make the sequence of operators symmetric to provide formal second order accuracy in τ. It is equally valid to apply L_η twice and L_ξ once, but it is more efficient to apply least often the operator requiring the most computational effort. Unfortunately, this decision may not be optimal if stability considerations dictate that the operator with the more severely restricted stability condition be applied over the smallest step size interval ($\Delta\tau/2$). This is precisely the sequence used for the coarse mesh in the original computer code. For the fine mesh, however, the L_η operator is broken up into a hyperbolic part involving only inviscid terms and a parabolic part involving the viscous contribution. The resulting sequence is given by

$$\Phi^{n-1} = L_\eta^h\left(\frac{\Delta\tau}{2}\right) L_\eta^p\left(\frac{\Delta\tau}{2}\right) L_\xi(\Delta\tau)\, L_\eta^p\left(\frac{\Delta\tau}{2}\right) L_\eta^h\left(\frac{\Delta\tau}{2}\right) \Phi^n \tag{20}$$

The operator L_η^h uses an approximation to the method of characteristics to solve the equation

$$\frac{\partial\Phi}{\partial\tau} + \frac{\partial F_i}{\partial\eta} = 0 \tag{21}$$

where $F_i = f_i + \eta_x e_i$. It is shown in Section 4.0 that this approximation is troublesome when wall mass transfer is considered. The operator L_η^p solves the equation

$$\frac{\partial\Phi}{\partial\tau} = \frac{\partial F_v}{\partial\eta} \qquad \left(F_v = f_v + \eta_x e_v\right)$$

with an implicit technique which takes advantage of the parabolic nature of the equation.

Of course, the advantage of using the time-splitting technique is that a less severe stability limitation on the stepsize, $\Delta\tau$, is realized and the stability analyses are simplified because all operators are one-dimensional.

Since the only difference between the equations just described and Eq. (16) is the source term, h, and the extra source in the $\nabla.\vec{q}$ terms of e_v and f_v [see Eq. (7)], a simple method of incorporating these terms into the existing code is to add another operator to the time-split sequence just described. This operator solves the equation

$$\frac{\partial\Phi}{\partial\tau} + h + \delta = 0 \tag{22}$$

where δ is the contribution due to the source in $\nabla.\vec{q}$. Let this operator be denoted by $L^{h\delta}$ so that $\Phi^{m+1} = L^{h\delta}\Phi^{m}$ where the superscript m indicates a fractional step operation. Equation (22) could be solved in a number of different ways; however, it is most convenient and efficient to introduce the primitive variable vector as the new dependent variable set. The equation is then given by

$$\frac{\partial \psi}{\partial \tau} + h^{\xi} + h^{\eta} = 0 \tag{23}$$

where $\psi = (\varrho, u, v, p)^T$ and h^{ξ}, h^{η} are given by

$$h^{\xi} = \frac{1}{y}\begin{pmatrix} \rho v \\ -\nu v_{\xi} - \frac{1}{\rho}(\lambda v)_{\xi} \\ \left(2\nu + \frac{\lambda}{\rho}\right)\frac{v}{y} \\ -2(\gamma-1)\lambda v u_{\xi} + \gamma p v - (2\mu+\lambda)(\gamma-1)\frac{v^2}{y} \end{pmatrix} \tag{24}$$

$$h^{\eta} = \frac{1}{y}\begin{pmatrix} 0 \\ -\nu(u_{\eta} - \eta_x v_{\eta}) - \frac{\eta_x}{\rho}(\lambda v)_{\eta} \\ -2\nu v_{\eta} - \frac{1}{\rho}(\lambda v)_{\eta} \\ (1-\gamma)\left[2\lambda v(v_{\eta} + \eta_x u_{\eta}) + kT_{\eta}\right] \end{pmatrix} \tag{25}$$

and ν is the kinematic viscosity, μ/ϱ. The relation between Φ and ψ may be expressed as

$$\Phi = M\psi \tag{26}$$

where M is a simple nonlinear algebraic operator. In addition, the solution to Eq. (23) may be expressed as

$$\psi^{m+1} = L^{\psi}\psi^{m}$$

where L^{ψ} is an appropriate finite-difference operator. Since a clear distinction is apparent between terms involving $\partial/\partial\eta$ operations, $\partial/\partial\xi$ operations, and algebraic operations in Eqs. (24) and (25), the operator L^{ψ} is split into two parts so that

$$L^{\psi} = L^{\psi}_{\xi} L^{\psi}_{\eta}$$

where the $\partial/\partial\eta$ terms are contained in L_η^ψ and the rest of the terms are contained in L_ξ^ψ. The operator L_ξ^ψ solves the equation

$$\frac{\partial \psi}{\partial \tau} + h^\xi = 0 \tag{27}$$

and L_η^ψ solves

$$\frac{\partial \psi}{\partial \tau} + h^\eta = 0 \tag{28}$$

The fractional step from m to m + 1 is thus expressed as

$$\psi^{m+1} = L_\xi^\psi L_\eta^\psi \psi^m$$

which is written with the use of Eq. (26) as

$$M^{-1}\Phi^{m+1} = L_\xi^\psi L_\eta^\psi M^{-1}\Phi^m$$

Premultiplying by M yields

$$\Phi^{m+1} = M L_\xi^\psi L_\eta^\psi M^{-1}\Phi^m$$

Thus, for the fine grid, the entire operator sequence for one symmetric step is given with reference to Eq. (20) as

$$\Phi^{n+1} = L_\eta^h\left(\frac{\Delta\tau}{2}\right)L_\eta^p\left(\frac{\Delta\tau}{2}\right)ML_\xi^\psi\left(\frac{\Delta\tau}{2}\right)L_\eta^\psi\left(\frac{\Delta\tau}{2}\right)M^{-1}L_\xi(\Delta\tau)ML_\eta^\psi\left(\frac{\Delta\tau}{2}\right)L_\xi^\psi\left(\frac{\Delta\tau}{2}\right)M^{-1}L_\eta^p\left(\frac{\Delta\tau}{2}\right)L_\eta^h\left(\frac{\Delta\tau}{2}\right)\Phi^n \tag{29}$$

An extension of Eq. (19) for the coarse grid is given by

$$\Phi^{n+1} = L_\xi\left(\frac{\Delta\tau}{2}\right)ML_\xi^\psi\left(\frac{\Delta\tau}{2}\right)L_\eta^\psi\left(\frac{\Delta\tau}{2}\right)M^{-1}L_\eta(\Delta\tau)ML_\eta^\psi\left(\frac{\Delta\tau}{2}\right)L_\xi^\psi\left(\frac{\Delta\tau}{2}\right)M^{-1}L_\xi\left(\frac{\Delta\tau}{2}\right)\Phi^n \tag{30}$$

The numerical details of the operators L_ξ^ψ and L_η^ψ are now presented.

A closer look at Eq. (27) reveals a useful structure of this system which is exploited in the development of the operator L_ξ^ψ. Substitution of Eq. (24) into Eq. (27) yields a partial uncoupling of the system of equations. In particular, the first and third components of this system are written as

$$\begin{aligned} \rho_\tau &= -\frac{\rho v}{y} \\ v_\tau &= -\frac{(2\mu+\lambda)}{y^2}\frac{v}{\rho} \end{aligned} \tag{31}$$

If it is assumed that μ and λ are time invariant, these equations represent a system of first order ordinary differential equations in the variables ρ and v. The second component of Eq. (27) is given by

$$u_\tau = \frac{1}{y}\left[\frac{\mu}{\rho} v_\xi + \frac{1}{\rho}(\lambda v)_\xi\right] \tag{32}$$

This equation is also an ordinary differential equation and is solved for u very easily since the entire RHS is known once the system represented by Eq. (31) is solved for ρ and v. The fourth component of Eq. (27) is

$$p_\tau + \frac{\gamma v}{y} p = \frac{\gamma - 1}{y}\left[2\lambda v u_\xi + (2\mu + \lambda)\frac{v^2}{y}\right] \tag{33}$$

Again, the RHS is known and the coefficient of p is a known function of τ (known numerically), so another ordinary differential equation results — this time for the pressure, p. Equations (31) through (33) may be easily solved numerically and variations in μ and λ are accounted for by using a predictor-corrector algorithm. That is, the equations are solved as described with current μ and λ values. The μ and λ values are then updated based on this solution and the corrector step is taken. Central differences are used for all spatial derivatives. This is a rapid second-order accurate procedure which describes the operator L_ξ^{ψ}.

The operator L_η^{ψ} which solves Eq. (28) is now described. The first component of this vector equation is

$$\frac{\partial \rho}{\partial \tau} = 0$$

which is trivially solved at each point with ρ = constant during this step. The remaining three equations are solved using MacCormack's standard one-dimensional scheme. These three equations are

$$\frac{\partial u}{\partial \tau} - \frac{1}{\rho y}\left[\mu(u_\eta + \eta_x v_\eta) + \eta_x(\lambda v)_\eta\right] = 0$$

$$\frac{\partial v}{\partial \tau} - \frac{1}{\rho y}\left[2\mu v_\eta + (\lambda v)_\eta\right] = 0$$

$$\frac{\partial p}{\partial \tau} - \frac{\gamma - 1}{y}\left[2\lambda v(v_\eta + \eta_x u_\eta) + kT_\eta\right] = 0$$

Let the superscript p denote the predicted value and the superscript c denote the corrected value, with no superscript indicating the current value. The numerical scheme for solving these equations is then given as

predictor

$$\rho_j^p = \rho_j$$

$$u_j^p = u_j + \frac{2\Delta r}{\rho_j y_j (y_{j+1} - y_{j-1})} \left[\mu_j \left[u_j - u_{j-1} + \eta_x (v_j - v_{j-1}) \right] + \eta_x (\lambda_j v_j - \lambda_{j-1} v_{j-1}) \right]$$

$$v_j^p = v_j + \frac{2\Delta r}{\rho_j y_j (y_{j+1} - y_{j-1})} \left[2\mu_j (v_j - v_{j-1}) + \lambda_j v_j - \lambda_{j-1} v_{j-1} \right]$$

$$p_j^p = p_j + \frac{2\Delta r(\gamma - 1)}{y_j (y_{j+1} - y_{j-1})} \left[2\lambda_j v_j \left[v_j - v_{j-1} + \eta_x (u_j - u_{j-1}) \right] + k_j (T_j - T_{j-1}) \right]$$

intermediate

$$T_j^p = \frac{p_j^p}{c_v \rho_j^p (\gamma - 1)}$$

$$\mu_j^p = f_1 \left(T_j^p \right)$$

$$k_j^p = \frac{\mu_j^p c_p}{Pr}$$

$$\lambda_j^p = f_2 \left(\mu_j^p \right)$$

corrector

$$\rho_j^c = \frac{1}{2} \left(\rho_j + \rho_j^p \right) = \rho_j$$

$$u_j^c = \frac{1}{2} \left\{ u_j^p + u_j + \frac{2\Delta r}{\rho_j y_j (y_{j+1} - y_{j-1})} \left[\mu_j^p \left[u_{j+1}^p - u_j^p + \eta_x \left(v_{j+1}^p - v_j^p \right) \right] + \eta_x \left(\lambda_{j+1}^p v_{j+1}^p - \lambda_j^p v_j^p \right) \right] \right\}$$

$$v_j^c = \frac{1}{2} \left\{ v_j^p + v_j + \frac{2\Delta r}{\rho_j y_j (y_{j+1} - y_{j-1})} \left[2\mu_j^p \left(v_{j-1}^p - v_j^p \right) + \lambda_{j+1}^p v_{j+1}^p - \lambda_j^p v_j^p \right] \right\}$$

$$p_j^c = \frac{1}{2} \left\{ p_j^p + p_j + \frac{2\Delta r(\gamma - 1)}{y_j (y_{j-1} - y_{j-1})} \left[2\lambda_j^p v_j^p \left[v_{j+1}^p - v_j^p + \eta_x \left(u_{j+1}^p - u_j^p \right) \right] + k_j^p \left(T_{j-1}^p - T_j^p \right) \right] \right\}$$

This scheme identifies the operator L_η^ψ.

At this point the two additional operators L_ξ^ψ and L_η^ψ have been described; however, their effect upon the stability of the entire sequence of operators must be determined.

3.3 STABILITY

A sufficient condition for the stability of the entire sequence of operators is that each operator in the sequence be stable. Therefore, it is enough to determine the conditions required for each of the operators L_ξ^ψ and L_η^ψ to be stable since MacCormack (Ref. 2) has given stability conditions for the other operators in the sequence.

For the operator L_ξ^ψ, consider a slightly different form of Eq. (27) written as

$$\frac{\partial \psi}{\partial \tau} + A \frac{\partial \psi}{\partial \xi} + s = 0$$

where A is a Jacobian matrix given by

$$A = \begin{pmatrix} 0 & 0 & 0 & 0 \\ 0 & 0 & -\frac{1}{y}(\nu + \nu') & 0 \\ 0 & 0 & 0 & 0 \\ 0 & -\frac{2(\gamma-1)\lambda v}{y} & 0 & 0 \end{pmatrix}$$

with $\nu' = \lambda/\rho$ and s is a collection of nonderivative terms*. The eigenvalues of the matrix A indicate the character of the equations. These eigenvalues, denoted by σ, are all zero. Since the well-known CFL (Courant, Friedrichs, Lewy) stability condition states that the maximum allowable step size, $\Delta\tau$, depends on the maximum eigenvalue of the Jacobian matrix through the relation

$$\Delta\tau \leq \frac{\Delta\xi}{|\sigma|_{max}}$$

this clearly implies that any $\Delta\tau$, which satisfies the stability requirement of the other operators will satisfy the requirement for the L_ξ^ψ operation. This result is consistent with the fact that this system reduces to a group of ordinary differential equations.

---

*Spatial variations in the second coefficient of viscosity, λ, are neglected in this analysis.

Now consider the following form of Eq. (28) for the L_η^ψ operator:

$$\frac{\partial \psi}{\partial \tau} + A \frac{\partial \psi}{\partial \eta} + s = 0$$

where A is given by

$$A = \begin{pmatrix} 0 & 0 & 0 & 0 \\ 0 & -\frac{\nu}{y} & -\frac{\eta_x}{y}(\nu + \nu') & 0 \\ 0 & 0 & -\frac{1}{y}(2\nu + \nu') & 0 \\ \frac{ka^2}{y c_p} & \frac{2(1-y)\lambda\nu\eta_x}{y} & \frac{2(1-y)\lambda\nu}{y} & -\frac{k}{y\rho c_v} \end{pmatrix}$$

where $a^2 = \gamma p/\gamma$. The eigenvalues of this matrix are

$$\sigma_1 = 0 \ , \ \sigma_2 = -\frac{\nu}{y} \ , \ \sigma_3 = -\frac{1}{y}(2\nu + \nu') \ , \ \sigma_4 = -\frac{k}{y\rho c_v}$$

In practice, $\lambda = -2/3\,\mu$ so that $\nu' = -2/3\,\nu$ and $\sigma_3 = -4/3\,\nu/y$. Therefore $|\sigma_3| > |\sigma_2|$. Also, $k/\rho c_v = \gamma\nu/Pr$ where Pr is the Prandtl number. Thus, σ_4 becomes $-\gamma\nu/(yPr)$. The maximum magnitude, $|\sigma|_{max}$, is then given by

$$|\sigma|_{max} = \max_{i,j}\left[\max\left(\frac{1}{y}\frac{\gamma\nu}{Pr} \ , \ \frac{4}{3}\frac{\nu}{y}\right)\right]$$

$$= \max\left(\frac{\gamma}{Pr} \ , \ \frac{4}{3}\right)\max_{i,j}\left(\frac{\nu}{y}\right)$$

The quantity γ/Pr will typically be larger than 4/3 so the maximum $\Delta\tau$ due only to this operator is restricted by the inequality

$$\Delta\tau \leq \frac{\Delta\eta}{\left(\frac{\nu}{y}\right)_{max}}\left(\frac{Pr}{\gamma}\right)$$

It has been found in practice that this stability condition is typically several orders of magnitude less restrictive than the condition which already exists, due to the other operators in the sequence. Therefore the present method of introducing the axisymmetric source terms into the existing computer code is a very effective one.

In addition to generalizing the computer code for application to axisymmetric flow problems, a portion of the current effort involves modification of the boundary conditions to allow simulation of wall mass transfer. This the subject of the next section.

4.0 WALL MASS TRANSFER

4.1 WALL BOUNDARY CONDITIONS

Some motivation for desiring an option to include effects of wall mass transfer is given in Section 1.0. This option normally requires a simple modification to the conventional conditions applied at a solid boundary. Unfortunately, an additional modification is required in the present application because of an implicit assumption in the original development of the code regarding the magnitude of the wall-normal flow velocity in the fine mesh. This modification is considered a major one and will be discussed following the description of the new wall boundary condition procedures.

Let m_i be the normal mass flux to be specified at the i^{th} point along the solid boundary grid line (see Fig. 4). Then

$$m_i = \rho_{i,w} V_{i,w}$$

where $V_{i,w}$ is the flow velocity normal to this boundary and $\varrho_{i,w}$ indicates the wall density at this point. Then the actual boundary condition procedure is similar to that described in Section 3.0 by Eqs. (11) through (15). That is, for $i < i_{\ell.e.}$ Eq. (11) applies. For $i \geq i_{\ell.e.}$ Eq. (13) or (14) still applies for the static temperature at the reflection line. However, Eq. (12) is modified to the following form:

$$\rho_{i,1} v_{i,1} = 2\rho_{i,w} v_{i,w} - \rho_{i,2} v_{i,2}$$

$$\rho_{i,1} u_{i,1} = 2\rho_{i,w} u_{i,w} - \rho_{i,2} u_{i,2}$$

where $u_{i,w} = -V_{i,w} \sin \theta_i$ and $v_{i,w} = V_{i,w} \cos \theta_i$ and θ_i is defined by Eq. (15). Substitution yields

$$\begin{aligned} \rho_{i,1} v_{i,1} &= 2m_i \cos \theta_i - \rho_{i,2} v_{i,2} \\ \rho_{i,1} u_{i,1} &= -2m_i \sin \theta_i - \rho_{i,2} u_{i,2} \end{aligned} \tag{34}$$

These equations allow the calculation of the quantities $\varrho_{i,1} v_{i,1}$ and $\varrho_{i,1} u_{i,1}$ but the value of $\varrho_{i,1}$ is needed in order to determine $u_{i,1}$ and $v_{i,1}$. This is accomplished by a simple iteration.

First assume that $p_{i,1} = p_{i,2}$. This simulates $\partial p/\partial n = 0$ at the solid wall. Then $T_{i,1}$ is known from Eq. (13) or (14). Thus, the equation of state

$$\rho_{i,1} = \frac{p_{i,1}}{(\gamma - 1)c_v T_{i,1}} \tag{35}$$

gives an estimate of $\rho_{i,1}$ which, with the use of Eq. (34) yields $u_{i,1}$, $v_{i,1}$. Now Eq. (17) is solved by applying Eq. (18) to yield an improved value for $p_{i,1}$. Then Eq. (35) improves $\rho_{i,1}$. This loop is repeated as necessary. In practice, two iterations are sufficient.

4.2 MODIFICATION TO HYPERBOLIC FINE MESH OPERATOR

The operator which solves Eq. (21) governing the inviscid contribution in the fine mesh is called L_η^h. This operator was originally developed based on the assumption that $V << a$ in the fine mesh where a is the sound speed. The author has reservations about the validity of this assumption for some hypersonic compression corner flows with separation and *no* wall mass transfer. For arbitrary wall mass transfer, this assumption is clearly invalid. It is therefore necessary to reformulate the operator L_η^h. Following the development of MacCormack (Ref. 2), Eq. (21) is expressed as

$$\psi'_\tau + A\psi'_\eta = 0 \tag{36}$$

where $\psi' = (\rho, U_c, V_c, p)^T$, $U_c = u$, $V_c = v + \eta_x u$ and

$$A = \begin{pmatrix} V_c & 0 & \rho & 0 \\ 0 & V_c & 0 & \eta_x/\rho \\ 0 & 0 & V_c & \dfrac{1+\eta_x^2}{\rho} \\ 0 & 0 & \gamma p & V_c \end{pmatrix}$$

U_c and V_c are the contravariant velocity components in the computational coordinates. The compatibility equations for this hyperbolic system are given by

$$\frac{dp}{dJ^+} + \frac{\rho c}{1+\eta_x^2}\frac{dV_c}{dJ^+} = 0 \qquad \text{along } J^- = \text{constant} \tag{37}$$

$$\frac{dp}{dJ^-} - \frac{\rho c}{1+\eta_x^2}\frac{dV_c}{dJ^-} = 0 \qquad \text{along } J^+ = \text{constant} \tag{38}$$

where $c = a\sqrt{1 + \eta_x^2}$ and J^+ and J^- are characteristic coordinates illustrated in Fig. 5. These equations are identical to those given by MacCormack even though his were obtained after assuming that $V_c << a$. The objective for the operator L_η^h is to determine the time-averaged convection and pressure fields for the time step of interest using the method of characteristics. The conventional MacCormack scheme is then applied to Eq. (21) using

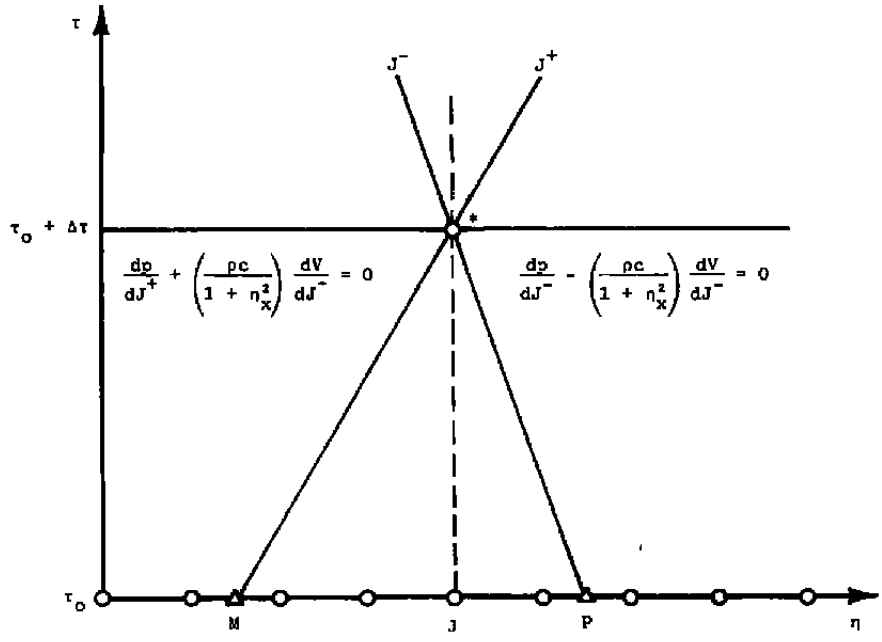

Figure 5. Characteristic coordinates.

these time-averaged values of V_c and p instead of the local values. This method greatly enhances the stability characteristics of the operator. This operator is applied at a given ξ station and in the τ-η plane. Let an overbar denote a time-averaging operation. Then $\overline{p}_j$, $\overline{V}_{cj}$ are the desired quantities. They are obtained by simply integrating their gradients to obtain

$$\overline{p}_j = \overline{p}_{j-1} + \int_{\eta_{j-1}}^{\eta_j} \left(\frac{\overline{dp}}{d\eta} \right) d\eta$$

$$\overline{V}_{c_j} = \overline{V}_{c_{j-1}} + \int_{\eta_{j-1}}^{\eta_j} \left(\frac{\overline{dV_c}}{d\eta} \right) d\eta$$

for $j > 2$ and

$$\bar{p}_2 = \bar{p}_{wall} + \int_0^{\eta_2} \left(\frac{\overline{dp}}{d\eta} \right) d\eta$$

$$\bar{V}_{c_2} = \bar{V}_{c_{wall}} + \int_0^{\eta_2} \left(\frac{\overline{dV_c}}{d\eta} \right) d\eta$$

with $\bar{p}_{wall} = .5 \left[.5 (p_{1,1} - p_{1,2}) + p_w \right]$ and $\bar{V}_{c_{wall}} = m_i/(\rho_{1,w} \cos\theta_1)$ and p_w is obtained by integrating Eq. (38) along the J^- characteristic to the wall. The quantities $\overline{\partial p/\partial \eta}$ and $\overline{\partial V_c/\partial \eta}$ are obtained from

$$\overline{\frac{\partial p}{\partial \eta}} = \frac{1}{\Delta\tau} \int_{\tau_a}^{\tau_a + \Delta\tau} \frac{\partial p}{\partial \eta} \, d\tau \tag{39}$$

$$\overline{\frac{\partial V_c}{\partial \eta}} = \frac{1}{\Delta\tau} \int_{\tau_b}^{\tau_b - \Delta\tau} \frac{\partial V_c}{\partial \eta} \, d\tau \tag{40}$$

where $\partial p/\partial \eta$ and $\partial V_c/\partial \eta$ are expressed in terms of derivatives with respect to τ by examining the last two components of Eq. (36) given by

$$V_{c_\tau} + V_c V_{c_\eta} + \left(\frac{1 + \eta_x^2}{\rho} \right) p_\eta = 0$$

$$p_\tau + \gamma p V_{c_\eta} - V_c p_\eta = 0$$

These equations may be expressed as $Q_\tau + B Q_\eta = 0$ where

$$Q = (V_c \ , \ p)^T \qquad \text{and}$$

$$B = \begin{pmatrix} V_c & \dfrac{1 + \eta_x^2}{\rho} \\ \gamma p & V_c \end{pmatrix}$$

Thus, Q_η = is given by $Q_\eta = -B^{-1} Q_\tau$ where

$$B^{-1} = \frac{1}{V_c^2 - c^2} \begin{pmatrix} V_c & -\dfrac{1+\eta_x^2}{\rho} \\ -\gamma p & V_c \end{pmatrix}$$

By direct substitution, Eqs. (39) and (40) become

$$\overline{\frac{\partial p}{\partial \eta}} = \frac{1}{\Delta\tau} \int_{\tau_o}^{\tau_o + \Delta\tau} \left(\frac{\gamma p}{V_c^2 - c^2} V_{c_\tau} - \frac{V_c}{V_c^2 - c^2} p_\tau \right) d\tau$$

$$\overline{\frac{\partial V_c}{\partial \eta}} = \frac{1}{\Delta\tau} \int_{\tau_o}^{\tau_o + \Delta\tau} \left(\frac{1-\eta_x^2}{\rho\left(V_c^2 - c^2\right)} p_\tau - \frac{V_c}{V_c^2 - c^2} V_{c_\tau} \right) d\tau$$

which may be integrated analytically by expressing the coefficients of V_{c_τ} and p_τ in terms of a mean value over the interval of integration. For example, in the general case,

$$\int_a^b A(x)\, B(x)\, dx = A(\bar{x}) \int_a^b B(x)\, dx \qquad \text{where} \qquad a \le \bar{x} \le b$$

provided, of course, that B(x) is of one sign over the interval of integration. The result is

$$\overline{\frac{\partial p}{\partial \eta}} = \frac{1}{\Delta\tau} \left[\frac{\gamma p}{V_c^2 - c^2} \Bigg|_{\tau=\bar{\tau}_1} \int_{\tau_o}^{\tau_o + \Delta\tau} V_{c_\tau}\, d\tau - \frac{V_c}{V_c^2 - c^2} \Bigg|_{\tau=\bar{\tau}_2} \int_{\tau_o}^{\tau_o + \Delta\tau} p_\tau\, d\tau \right]$$

$$\overline{\frac{\partial V_c}{\partial \eta}} = \frac{1}{\Delta\tau} \left[\frac{1+\eta_x^2}{\rho\left(V_c^2 - c^2\right)} \Bigg|_{\tau=\bar{\tau}_3} \int_{\tau_o}^{\tau_o + \Delta\tau} p_\tau d\tau - \frac{V_c}{V_c^2 - c^2} \Bigg|_{\tau=\bar{\tau}_4} \int_{\tau_o}^{\tau_o + \Delta\tau} V_{c_\tau}\, d\tau \right]$$

and

$$\int_{\tau_o}^{\tau_o + \Delta\tau} V_{c_\tau}\, d\tau = V_c(\tau_o + \Delta\tau) - V_c(\tau_o)$$

$$\int_{\tau_o}^{\tau_o + \Delta\tau} p_\tau\, d\tau = p(\tau_o - \Delta\tau) - p(\tau_o)$$

The application of these equations at point j gives

$$\left(\overline{\frac{\partial p}{\partial \eta}}\right)_j = \frac{1}{\Delta\tau}\left[\left.\frac{\gamma p}{V_c^2 - c^2}\right|_j^{\tau_o+\frac{\Delta\tau}{2}}\left(V_c^* - V_{c_j}\right) - \left.\frac{V_c}{V_c^2 - c^2}\right|_j^{\tau_o+\frac{\Delta\tau}{2}}\left(p^* - p_j\right)\right] \quad (41)$$

$$\left(\overline{\frac{\partial V_c}{\partial \eta}}\right)_j = \frac{1}{\Delta\tau}\left[\left.\frac{c^2}{\gamma p\left(V_c^2 - c^2\right)}\right|_j^{\tau_o+\frac{\Delta\tau}{2}}\left(p^* - p_j\right) - \left.\frac{V_c}{V_c^2 - c^2}\right|_j^{\tau_o+\frac{\Delta\tau}{2}}\left(V_c^* - V_{c_j}\right)\right] \quad (42)$$

where $p^* = p_j(\tau_o + \Delta\tau)$, $V_c^* = V_{c_j}(\tau_o + \Delta\tau)$ as shown in Fig. 5 and $\bar{\tau}_1$, $\bar{\tau}_2$, $\bar{\tau}_3$, $\bar{\tau}_4$, have been taken to be the interval midpoint. The unknowns p^*, V_c^* are determined by solving the compatibility equations [Eqs. (37) and (38)] along the appropriate characteristics. The finite-difference representations of Eqs. (37) and (38)] are given by

$$(p^* - p^M) + \left.\frac{\gamma p}{c}\right|^M \left(V_c^* - V_c^M\right) = 0$$

$$(p^* - p^P) - \left.\frac{\gamma p}{c}\right|^P \left(V_c^* - V_c^P\right) = 0$$

where the points indicated by superscripts P and M are illustrated in Fig. 5. These equations are easily solved for p^* and V_c^* to yield

$$p^* = \frac{\left.\frac{\gamma p}{c}\right|^P \left.\frac{\gamma p}{c}\right|^M \left(V_c^P - V_c^M\right) + \left.\frac{\gamma p}{c}\right|^P p^M + \left.\frac{\gamma p}{c}\right|^M p^P}{\left.\frac{\gamma p}{c}\right|^M + \left.\frac{\gamma p}{c}\right|^P}$$

$$V_c^* = \frac{p^P - p^M + \left.\frac{\gamma p}{c}\right|^M V_c^M + \left.\frac{\gamma p}{c}\right|^P V_c^P}{\left.\frac{\gamma p}{c}\right|^M + \left.\frac{\gamma p}{c}\right|^P}$$

It is important to note that Eqs. (41) and (42) are different from those obtained by MacCormack (Ref. 2) due to his assumption $V_c << a$. In particular, the terms with coefficients $V_c/(V_c^2 - c^2)$ were neglected by MacCormack. However, these terms must be included in the operator L_η^h because of the new wall mass transfer boundary condition.

The next section provides the results of various verification phases of the work presented herein. These results illuminate many of the same characteristics and, in some cases, deficiencies that exist for the original two-dimensional version of the computer code.

5.0 RESULTS AND DISCUSSION

All of the numerical results presented in this section are for a *hollow* cylinder-flare configuration in a Mach 2.98 freestream. The free-stream static temperature is 202.85°R and the unit Reynolds number is 10.97 million per foot.The assumed isothermal wall temperature is taken to be 520°R. The configuration is 28 in. from the cylinder leading edge to the cylinder-flare junction point; its outer radius is 5.97 in., and the flare angle is 25 deg. The flare length is about 5 in. This configuration was tested experimentally by Roshko and Thomke (Ref. 14). The numerical results of the present study are compared to these experimental results wherever possible.

5.1 CODE VERIFICATION

An initial flow solution is required to start a numerical calculation. Since a steady-state solution to the Navier-Stokes equations is sought, this initial solution is arbitrary within the limitation that it must be sufficiently smooth not to cause failure of the numerical algorithm. The computer code is designed to provide various options for performing this initialization. One of these options is used when a solution is desired over an *entire* cylinder-flare configuration. That is, the computational domain extends over the entire length of the configuration (see Fig. 6). The leading edge singularity is captured as part of the numerical

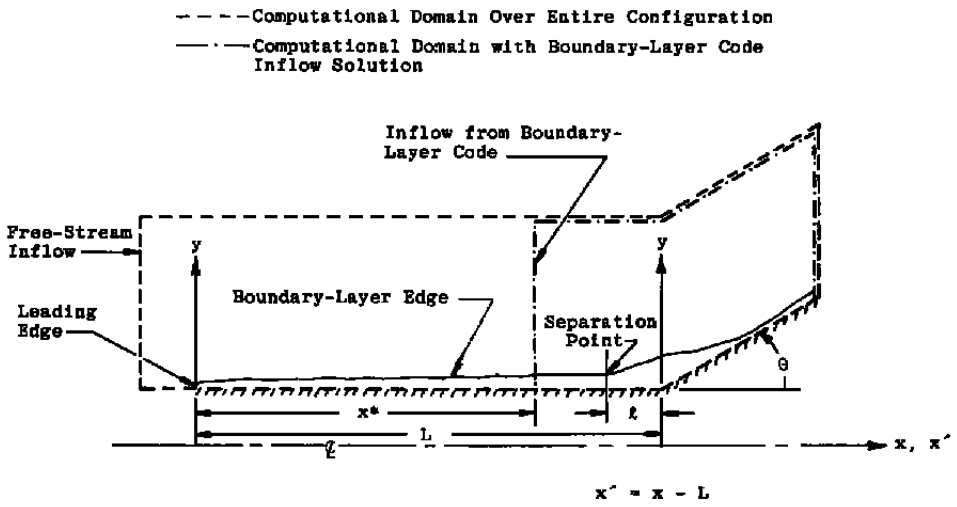

Figure 6. Initialization options.

solution. This option is used when the interaction region at the cylinder-flare corner extends upstream more than 20 percent of the distance to the leading edge. In this case the

interaction region is adequately described by several grid points. If this interaction extent is much less than 20 percent of the distance to the leading edge, then too few grid points are available to describe it and the flow field over the entire cylinder. In this case, a second option is used for initialization. That is, a solution is obtained at some x-location such as x*, well ahead of the interaction region using a boundary-layer code attributable to Patankar and Spalding (Ref. 22). This solution is then used to define an inflow boundary condition for the new computational domain which has this station, x*, as its left-most boundary. This option was used in the present study since the experimental data of Roshko and Thomke (Ref. 14) indicate an interaction length, ℓ, of about 1 in. *Thus the interaction extent is about 3.6 percent of the distance from the cylinder-flare corner to the cylinder leading edge. If the first initialization option were used, approximately 200 grid points would be required between the cylinder leading edge and the end of the flare to provide only six points within the interaction region (assuming equal grid point spacing in the x-direction). This is clearly an enormous waste of computational effort when the interest is in the interaction and its effect on the flare solution.

Figure 7 illustrates the actual finite-difference grid resulting from the use of the second initialization option. The abscissa, x', is measured from the cylinder-flare corner, and the

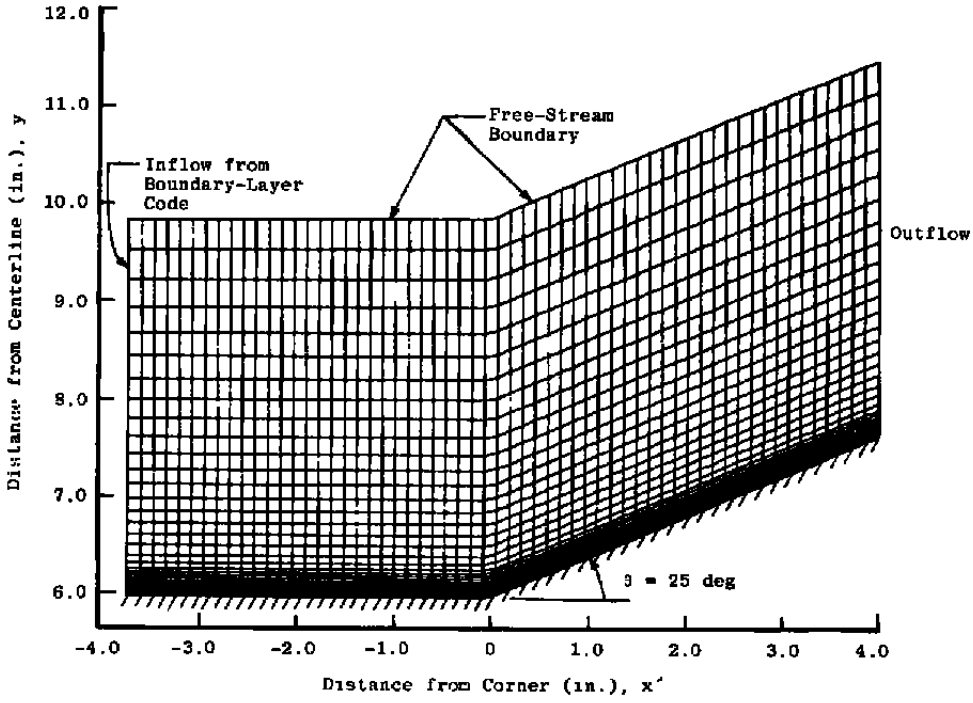

Figure 7. Actual finite-difference grid

*The interaction length is defined to be the distance from the beginning of the pressure rise to the corner (see Fig. 8b).

ordinate, y, is measured from the centerline. Note the heavy concentration of grid lines near the wall boundary to resolve the viscous-dominated flow features.

As part of the verification of the axisymmetric capability of the computer code, two numerical solutions were obtained at zero flare angle. These two solutions were obtained with the "current" turbulence model of Cebeci, Smith, and Mosinskis (Ref. 20) and the "alternate" turbulence model of Baldwin and Lomax (Ref. 21) (see Section 2.3 for a description of these models). The axial velocity profiles from these two solutions at station $x' = 0$ (obtained with $x^* \cong 0.8L$) are compared in Fig. 8a to the profile obtained from the Patankar-Spalding boundary- layer code at the same streamwise station. The solution obtained with the "alternate" turbulence model shows better agreement with the Patankar-Spalding profile than the solution obtained with the "current" turbulence model. For this reason and because the boundary-layer code has been verified against experimental data by Patankar and Spalding (Ref. 22), all subsequent calculations were made using the "alternate" turbulence model.

Additional verification of the axisymmetric capability of the computer code is illustrated in Fig. 8b. A comparison of surface pressure distributions on the actual hollow cylinder-flare configuration is shown here for the numerical solution and the experimental data of Roshko and Thomke (Ref. 14). The computed pressure rise and asymptotic value on the flare section agree well with the experimental data. The interaction extent for the numerical solution is about $\ell_{num} \cong 0.5$ in. while the experimental results suggest an extent of about $\ell_{exp} \cong 1$ in. Although this discrepancy is significant when the details of separation are of interest, it has nothing to do with the axisymmetric modification to the computer code. This comment is strongly supported by strikingly similar comparisons which are documented, for example, in Refs. 8, 9, and 10 for a number of two-dimensional problems. These references also indicate that improvements in the numerical solution result from the application of special ad hoc features to the turbulence models such as the so-called relaxation approach. It is beyond the scope of this effort, however, to experiment with such features.

It must be pointed out that the largest uncertainty in the state-of-the-art numerical solutions to high Reynolds number turbulent flows is attributable to the failure of the turbulence modeling effort to accurately reflect the physical turbulence characteristics of the flow. A great deal of research is currently being devoted to this turbulence modeling problem worldwide because of the important role of turbulence in modern aerodynamics design work.

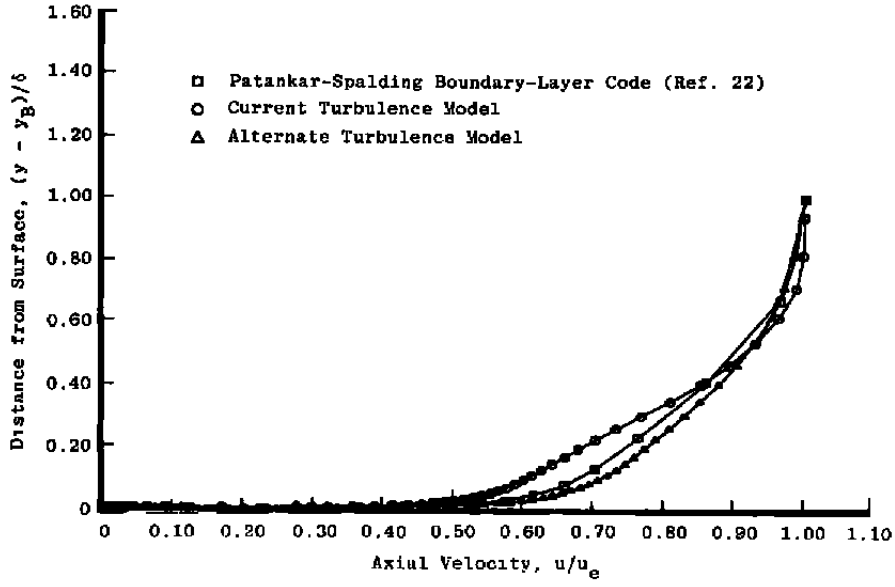

a. Velocity profiles at $x' = 0$ for zero flare angle condition

Figure 8. Test of computer code on a simple axisymmetric turbulent boundary layer.

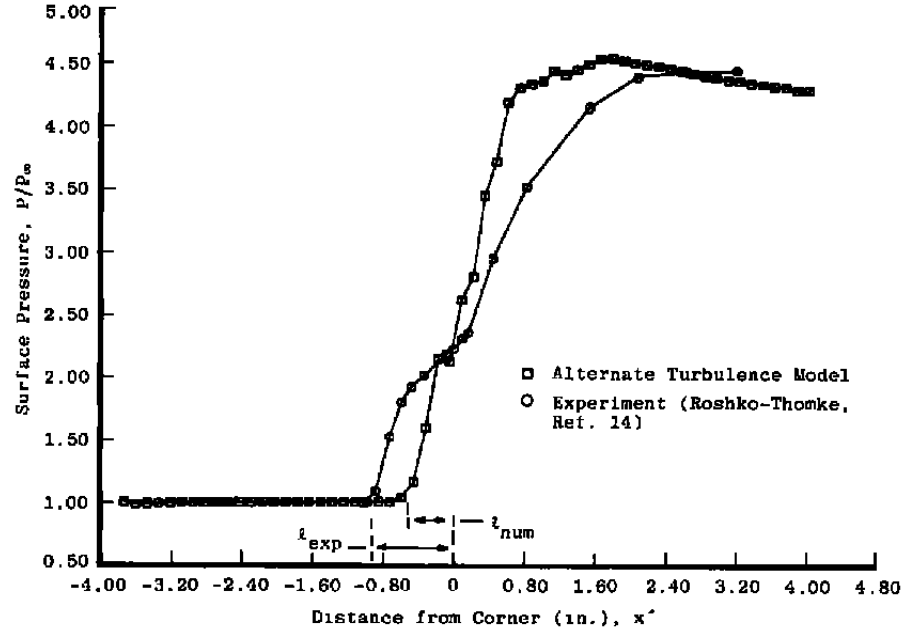

b. Cylinder-flare surface pressure distribution

Figure 8. Concluded.

5.2 FLOW-FIELD DETAILS

This section illustrates some details of the shock-induced separated flow field with the use of Figs. 9a through d. Figure 9a shows contours of stream function which clearly illustrate the recirculation zone and the flow lift-off occurring near the separation point. The wiggles appearing in these contours are caused by numerical "noise" in the solution in the vicinity of the compression corner. These wiggles appear in spite of the use of a product fourth order artificial viscosity term by Hung and MacCormack (Ref. 1). It is important to note that the recirculation bubble serves as a sharp turn smoothing device which converts an abrupt compression corner into a gradual compression followed by a gradual expansion followed by another less gradual compression. The streamlines over the separation bubble illustrate this behavior.

An illustration of the velocity profiles showing the onset of reversed flow (separation) and reattachment is given in Fig. 9b. Note the full profile at $x' = -0.45$ in. In contrast to this profile, the profile at $x' = +0.6$ in. behind the separation zone is not full. In fact, the flow does not develop into a full profile behind the separation zone until it reaches about half way back on the flare (i.e., $x' \cong 2.0$ in.).

The shock structure is illustrated by static pressure contours (isobars) in Fig. 9c. The shock, which is a physical discontinuity for all practical purposes, is shown to be smeared out in this figure. This is attributable to the application of the so-called shock-capturing approach in which no special provision is made in the computer code for the existence of such discontinuities. If they exist, they are "captured" by the numerical scheme. A key feature of this figure is the manner in which the contour lines all approach the wall in a near-normal direction. This implies that $\partial p/\partial n = 0$ at the wall and in a region near the wall. This is consistent with boundary-layer theory which is perhaps fortuitous since it contrasts with the experimental results of Settles, Vas, and Bogdonoff (Ref. 7) who show contrary results near the reattachment region for a two-dimensional case.

Figure 9d is a simple contour of the flow sonic line. This figure illustrates how abruptly the subsonic zone grows in height at the separation point, yet its retreat back near the wall is asymptotic and requires over half the flare length to reach a relative height equivalent to its height just ahead of separation. This is consistent with the fact that full velocity profiles in the boundary layer develop slowly after reattachment of the flow.

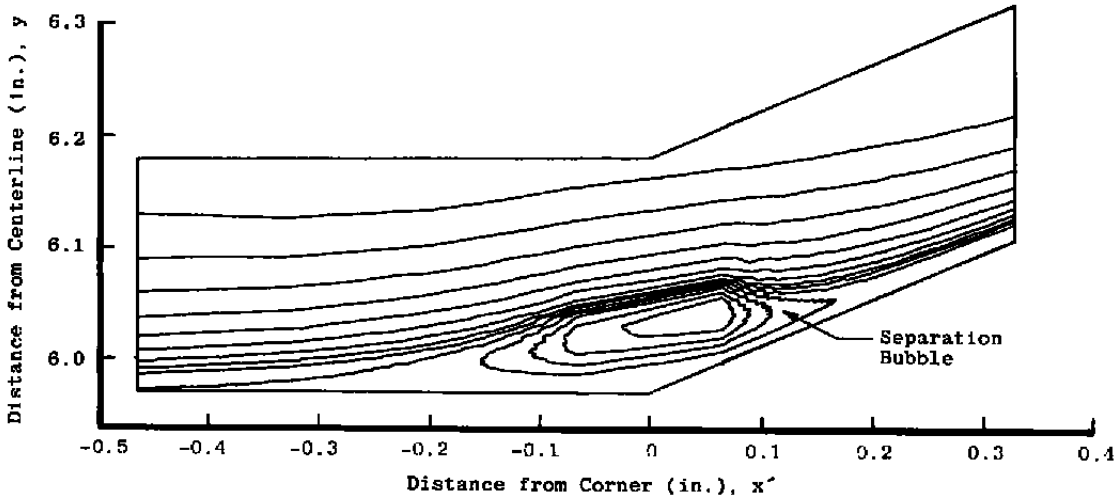

a. Streamlines

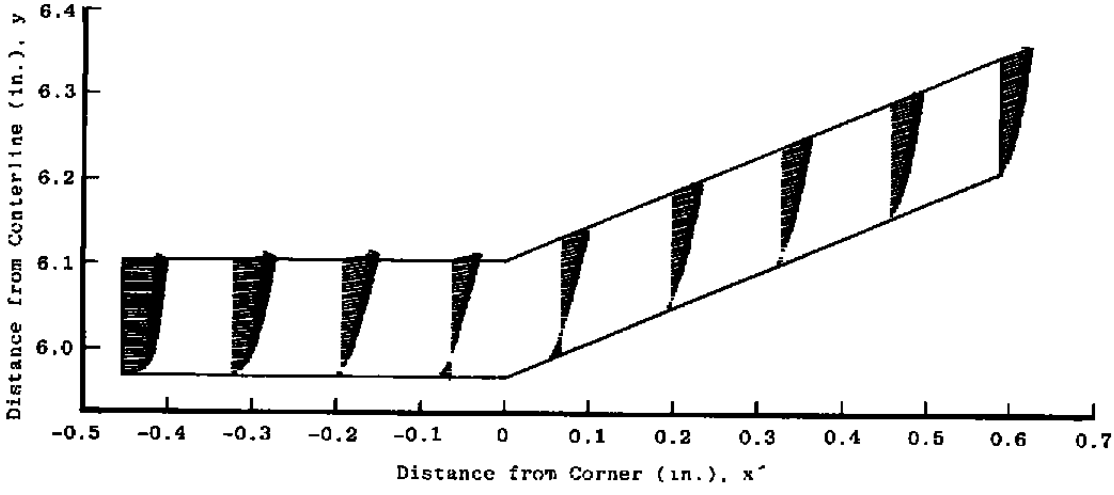

b. Velocity vectors

Figure 9. Illustration of computed separation, reversed flow, and shock boundary-layer interaction.

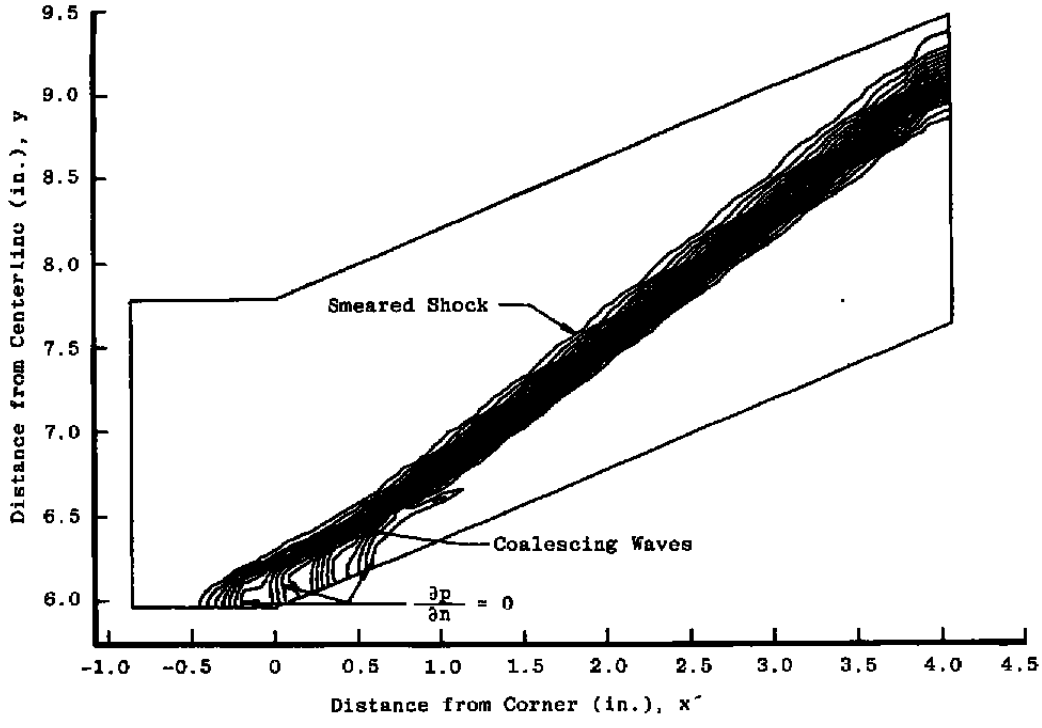

c. Static pressure contours

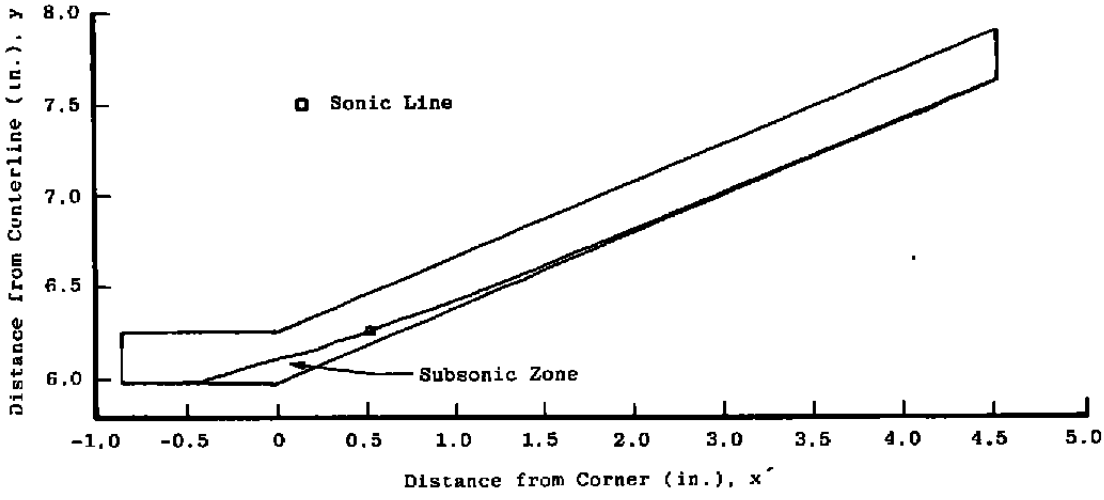

d. Sonic line contour

Figure 9. Concluded.

5.3 EFFECTS OF WALL MASS TRANSFER

The wall mass transfer option required extensive modification to the computer code as mentioned in Section 4.0. This modified code was first verified by solving the hollow cylinder-flare configuration with zero wall mass transfer. These results were expected to compare favorably with the numerical solution shown in Fig. 8b. Figure 10 illustrates that this is indeed true. In fact, the code with the wall mass transfer modifications produced a solution which is slightly closer to the experimental data of Roshko and Thomke than the solution from the code without these modifications. The slight difference between the two numerical solutions is caused by the modifications made to the hyperbolic fine mesh operator and to the wall boundary conditions described in Section 4.0.

The next test was to introduce suction into the cylinder-flare corner and qualitatively analyze the results. The wall-normal mass flux for this test was taken to be $-0.01\ \rho_e u_e$ where $\rho_e u_e$ is the axial mass flux at the edge of an undisturbed boundary layer 28 in. long (the length of the cylinder portion), and the negative sign indicates suction rather than blowing. This normal flux was applied at one point on each side of the cylinder-flare corner (there is no point exactly at the corner), giving an axial suction extent of 0.13 in. on each side of the corner. A reduction in the size of the separation region was expected from this suction. Figure 11 illustrates that about a 30 percent reduction did result, and the intermediate pressure plateau which appeared between -0.25 in. $\leq x' \leq 0.25$ in. for the zero wall mass transfer case vanished. The solution away from the corner is unaffected by the suction. As mentioned, this test is qualitative in nature. Further testing of this option is needed for a laminar case for which experimental data are available and where the uncertainty attributable to turbulence modeling is eliminated.

6.0 CONCLUDING REMARKS

The computer code documented in Refs. 1 and 2 by Hung and MacCormack was extended to apply to axisymmetric flows over cylinder-flare shapes. Two new operators developed for this extension were added to the existing time-split sequence of operators. The operator L_η^ψ, which involves radial derivative term contributions to the complete axisymmetric source term group, was found to have an upper stability bound on the step size, $\Delta\tau$, which is governed by the CFL condition. This bound is proportional to the Prandtl number and inversely proportional to the ratio of thermal capacities of the fluid, γ, times the maximum value over all grid points of the kinematic viscosity scaled by the radial coordinate (see Section 3.3). It was found in practice that this stability bound was several orders of magnitude less restrictive for the cylinder-flare problem examined in this study than bounds already present attributable to the other operators in the sequence; however, this may not

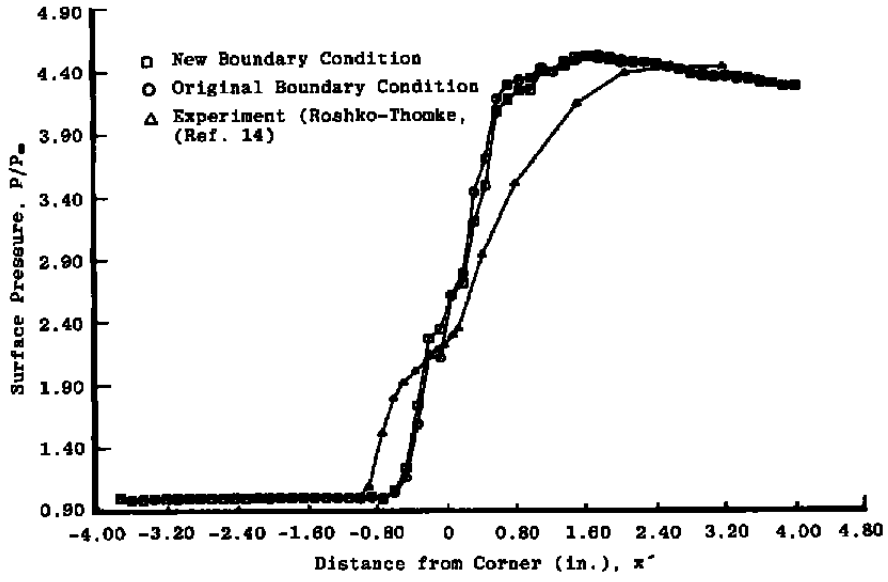

Figure 10. Verification of new wall mass transfer boundary condition and associated operator L_η^h for the case of zero wall mass transfer.

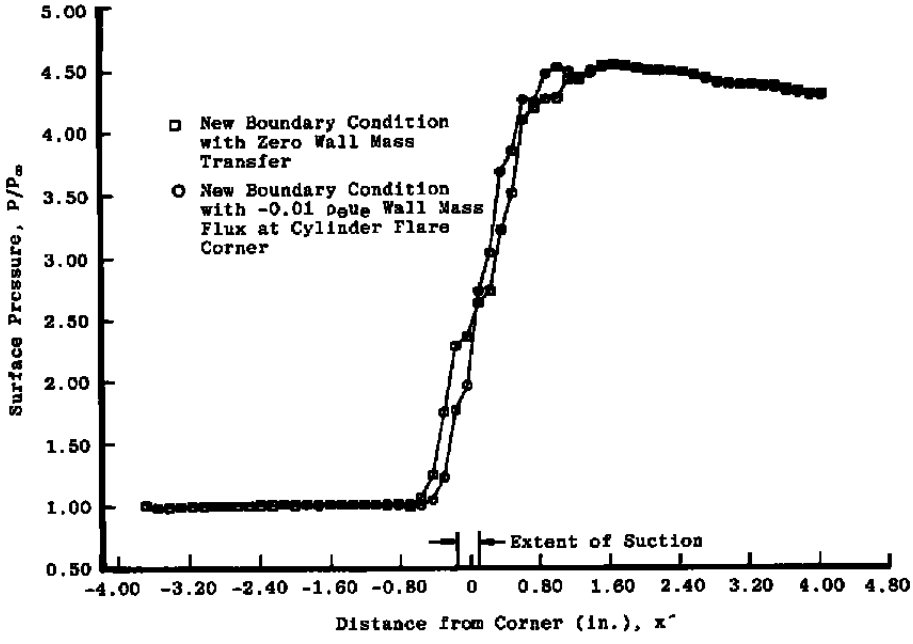

Figure 11. Effect of suction at the cylinder-flare junction.

always be the case. Two algebraic eddy viscosity turbulence models were described and tested. The model of Cebeci, Smith, and Mosinskis (Ref. 20) was discarded in favor of the Baldwin-Lomax model (Ref. 21) based on comparisons made with a boundary-layer solution from the code of Patankar and Spalding (Ref. 22). Additionally the computer code was modified to allow for the option of wall mass transfer. This required development of a new hyperbolic fine mesh operator, L_η^h, because of the assumption in the development of the original operator that $V << c$ in the fine mesh. The final computer code was verified by comparisons of boundary-layer profiles with those from the Patankar-Spalding code and by comparisons of surface pressure distributions with the experimental results of Roshko and Thomke (Ref. 14) for a particular hollow cylinder-flare configuration. The computed surface pressure distributions agree poorly in the separation region because of the inadequacies of the turbulence model, which is entirely consistent with computed results for two-dimensional flows over compression corners (e.g., see Refs. 8, 9, and 10). Flow-field details are presented illustrating shock structure, separation, and reattachment details as well as quick buildup and gradual decay of a subsonic pocket near the cylinder-flare corner. Qualitative effects of introducing suction into the cylinder-flare corner are presented and discussed.

The final computer code is considered applicable in general to flows over two-dimensional compression corners and/or cylinder-flare configurations at zero incidence. In particular, application should be limited to laminar flows with and without separation, and turbulent flows for which an eddy viscosity turbulence model adequately describes the flow physics. These problems may have suction or blowing at the wall.

Future effort is needed in several areas: first, the turbulence modeling problem is by far the most restrictive and should therefore be given the most attention; second, the code is designed for two specific geometric shapes — wall-ramp or cylinder-flare configurations. This constraint should be relaxed so the flow is computable over virtually any two-dimensional or axisymmetric shape; finally, the effects of a real, rather than a perfect, gas should be included to extend the code's ability to provide accurate answers to real engineering problems.

REFERENCES

1. Hung, C. M. and MacCormack, R. W. "Numerical Solutions of Supersonic and Hypersonic Laminar Flows Over a Two-Dimensional Compression Corner." AIAA Paper No. 75-2, AIAA 13th Aerospace Sciences Meeting, Pasadena, California, January 1975.

2. MacCormack, Robert W. "An Efficient Numerical Method for Solving the Time-Dependent Compressible Navier-Stokes Equations at High Reynolds Number." NASA TM X-73,129, July 1976.

3. Gray, J. Don and Rhudy, R. W. "Investigation of Flat-Plate Aspect Ratio Effects on Ramp-Induced, Adiabatic, Boundary-Layer Separation at Supersonic and Hypersonic Speeds." AEDC-TR-70-235, March 1971.

4. Bloy, A. W. and Georgeff, M. P. "The Hypersonic Laminar Boundary Layer Near Sharp Compression and Expansion Corners." *Journal of Fluid Mechanics*, Vol. 63, Part 3, 1974, pp. 431-447.

5. Carter, J. E. "Numerical Solutions of the Navier-Stokes Equations for the Supersonic Laminar Flow Over a Two-Dimensional Compression Corner." NASA TR R-385, July 1972.

6. Law, C. H. "Supersonic Shock Wave-Turbulent Boundary Layer Interactions." AIAA Paper No. 75-832, AIAA 8th Fluid and Plasma Dynamics Conference, Hartford, Connecticut, June 1975.

7. Settles, Gary S., Vas, Irwin E., and Bogdonoff, Seymour M. "Shock Wave-Turbulent Boundary Layer Interaction at a High Reynolds Number, Including Separation and Flowfield Measurements." AIAA Paper No. 76-164, AIAA 14th Aerospace Sciences Meeting, Washington, D.C., January 1976.

8. Shang, J. S. and Hankey, W. L., Jr. "Numerical Solution of the Navier-Stokes Equations for Supersonic Turbulent Flow Over a Compression Ramp." AIAA Paper No. 75-3, AIAA 13th Aerospace Sciences Meeting, Pasadena, California, January 1975.

9. Coakley, T. J., Viegas, J. R., and Horstman, C. C. "Evaluation of Turbulence Models for Three Primary Types of Shock-Separated Boundary Layers." AIAA Paper No. 77-692, AIAA 10th Fluid & Plasmadynamics Conference, Albuquerque, New Mexico, June 1977.

10. Horstman, C. C., Hung, C. M., Settles, G. S., Vas, I. E., and Bogdonoff, S. M. "Reynolds Number Effects on Shock-Wave Turbulent Boundary-Layer Interactions — A Comparison of Numerical and Experimental Results." AIAA Paper No. 77-42, AIAA 15th Aerospace Sciences Meeting, Los Angeles, California, January 1977.

11. Kuehn, Donald M. "Turbulent Boundary-Layer Separation Induced by Flares on Cylinders at Zero Angle of Attack." NASA TR R-117, 1961.

12. Polak, Arnold and Kalivretenos, Chris A. "Hypersonic Turbulent Boundary-Layer Separations at High Reynolds Numbers." *Journal of Spacecraft and Rockets*, Vol. 6, No. 8, August 1969, pp. 954-955.

13. Coleman, G. T. and Stollery, J. L. "Incipient Separation of Axially Symmetric Hypersonic Turbulent Boundary Layers." *AIAA Journal*, Vol. 12, No. 1, January 1974, pp. 119-120.

14. Roshko, A. and Thomke, G. J. "Flare-Induced Interaction Lengths in Supersonic, Turbulent Boundary Layers." *AIAA Journal*, Vol. 14, No. 7, July 1976, pp. 873-879.

15. Rosenhead, L. "A Discussion on the First and Second Viscosities of Fluids." *Proceedings of Royal Society*, Ser. A, Vol. 226, October 1954, pp. 1-64.

16. Owczarek, J. A. *Fundamentals of Gas Dynamics*. International Textbook Co., Scranton, PA, 1964.

17. Lamb, H. *Hydrodynamics*. Dover Publications, Inc., New York, 1945 (Sixth Edition).

18. Yuan, S. W. *Foundations of Fluid Mechanics*. Prentice-Hall, Inc., Englewood Cliffs, NJ, 1967.

19. Marvin, Joseph G. "Turbulence Modeling for Compressible Flows." NASA TM X-73,188, January 1977.

20. Cebeci, T., Smith, A. M. O., and Mosinskis, G. "Calculation of Compressible Adiabatic Turbulent Boundary Layers." *AIAA Journal*, Vol. 8, No. 11, November 1970, pp. 1974-1982.

21. Baldwin, B. and Lomax, H. "Thin-Layer Approximation and Algebraic Model for Separated Turbulent Flows." AIAA Paper No. 78-257, AIAA 16th Aerospace Sciences Meeting, Huntsville, Alabama, January 1978.

22. Patankar, S. V. and Spalding, D. B. *Heat and Mass Transfer in Boundary Layers, A General Calculation Procedure*. Intertext Books, London, 1970 (Second Edition).

NOMENCLATURE

A	Jacobian matrix used in stability analysis
A^+	van Driest's constant
a	Sound speed
B	Coefficient matrix used in development of new L_η^h
b	General constant in Klebanoff-type intermittency factor
C	Constant in outer-layer turbulence model
C_{CP}	Constant in Baldwin-Lomax turbulence model
C_{KLEB}	Specific Baldwin-Lomax constant for Klebanoff-type intermittency factor
C_{WK}	Baldwin-Lomax turbulence model wake constant
c	Geometry-scaled sound speed
c_p	Specific heat at constant pressure
c_v	Specific heat at constant volume
D	van Driest damping factor
E	Flux vector used in discussion of time-splitting
e, $\hat{e}$	Flux vectors
$\tilde{e}$	Specific internal energy
F	Flux vector used in discussion of time-splitting
f,$\hat{f}$	Flux vectors
f	Denotes functional dependence
G	Denotes a measure of local mass-weighted velocity gradient for turbulence models
g,$\hat{g}$	Flux vectors
H	Total mesh height

H_F	Fine mesh height
$\mathbf{h}, \hat{\mathbf{h}}$	Source term vectors
$\hat{i}$	Cartesian unit vector in x-direction
$\hat{i}_\xi, \hat{i}_\eta, \hat{i}_\zeta$	Curvilinear unit vectors in ξ, η, ζ directions, respectively
J^+, J^-	Characteristic coordinates in the fine mesh
$\hat{j}$	Cartesian unit vector in y-direction
K	Constant in Cebeci-Smith-Mosinskis turbulence model
k	Conductivity coefficient
$\hat{k}$	Cartesian unit vector in z-direction and constant in turbulence model mixing-length expression
L_ξ	Time-split finite-difference operator associated with ξ-direction
L_η	Time-split finite-difference operator associated with η-direction
L_η^h	Time-split finite-difference operator for hyperbolic terms in η-direction
L_η^p	Time-split finite-difference operator for parabolic terms in η-direction
$L^{h\delta}$	Time-split finite-difference operator for entire source term with conservative dependent variables
L^ψ	Time-split finite-difference operator for entire source term with primitive dependent variables
L_ξ^ψ	Portion of L^ψ associated with ξ-direction
L_η^ψ	Portion of L^ψ associated with η-direction
ℓ	Mixing length or separation interaction length
M	Nonlinear algebraic transformation matrix relating conservative variables to primitive variables
m	Mass flux

Pr	Prandtl number
p	Static pressure
Q	Klebanoff-type intermittency factor and dependent variable vector used in development of L_η^h
$\vec{q}$	Velocity vector
s	Source term vector
T	Static temperature
t	Time
U_c	Contravariant velocity component normal to ξ = constant lines
U_{DIF}	Parameter used in Baldwin-Lomax turbulence model
u	Axial velocity component
V	Wall-normal velocity component
V_c	Contravariant velocity component normal to η = constant lines
v	Velocity component in y-direction
w	Velocity component in z-direction
x	Axial direction
x′	Shifted axial coordinate
x*	Location of left-most grid boundary
y	Direction normal to axis
$\hat{y}$	Reference distance normal to the wall for turbulence model
y^+	Inner-law variable used in turbulence model
z	Cartesian coordinate
γ	Specific heat ratio

$\Delta\tau$	Temporal step size
$\Delta\xi$, $\Delta\eta$	Spatial computational mesh increments
δ	Boundary-layer thickness
δ^*	Displacement thickness
ϵ	Total energy per unit volume
ζ,η	Curvilinear coordinates in an axis-normal plane
θ	Ramp/flare angle
$\varkappa$	Bulk viscosity coefficient
λ	Second coefficient of viscosity
μ	First coefficient of viscosity
ν	Kinematic viscosity
ν'	Second coefficient of viscosity divided by density
ξ	Computational axial coordinate
ϱ	Density
σ	Eigenvalue
τ	Computational temporal coordinate
τ_r	Reference shear stress
Φ	Solution vector used in discussion of time-splitting
ϕ, $\hat{\phi}$	Solution vectors
ψ	Primitive variable vector
ψ'	Reduced primitive variable vector
ω	Vorticity
∇	Gradient operator

SUBSCRIPTS

B	Indicates body or wall value
c	Indicates corner value
e	Denotes edge value
i	Denotes inviscid or represents index in x-direction
j	Represents index in y-direction
ℓ	Denotes laminar quantity
ℓ.e.	Denotes leading edge
r	Denotes reference value
t	Denotes turbulent quantity; also indicates partial differentiation with respect to the independent variable, t
v	Denotes viscous
w	Indicates wall value
x	Indicates partial differentiation with respect to x
y	Indicates partial differentiation with respect to y
z	Indicates partial differentiation with respect to z
ζ	Indicates partial differentiation with respect to ζ
η	Indicates partial differentiation with respect to η
ξ	Indicates partial differentiation with respect to ξ
τ	Indicates partial differentiation with respect to τ

SUPERSCRIPTS

a, $\bar{a}$	Fractional step indicators
b, $\bar{b}$	Fractional step indicators
c	Denotes corrected value

h	Denotes hyperbolic
M	Denotes minus for the method of characteristics
m	General fractional step index
$n, \overline{n+1}, n+1$	Fractional step indicators
P	Denotes plus for the method of characteristics
p	Denotes parabolic or predicted value
T	Denotes transpose operation
η, ξ	Indicate source term groupings
*	Denotes solution point for the method of characteristics

OTHER

$(\bar{\ })$	Indicates association with Cartesian reference frame or denotes a time-averaged quantity
$(\hat{\ })$	Indicates association with cylindrical coordinates (except for unit vector and other specifically mentioned applications)
$(\ )\cdot(\ )$	Indicates dot product
$(\ )\times(\ )$	Indicates cross product